CHALMERS

Electromagnetic modeling of pacemaker lead heating during MRI

Technical report

Oskar Talcoth, Thomas Rylander

Department of Signals and Systems
CHALMERS UNIVERSITY OF TECHNOLOGY
Göteborg, Sweden

R014/2011
ISSN 1403-266X

Abstract

The electromagnetic part of pacemaker lead heating during magnetic resonance imaging (MRI) is a resonant phenomenon which is complicated by, among other factors, the wide range of length scales involved in the problem. In this work, the multi-scale part of the problem is taken into special consideration during the modeling process. The model incorporates a radio frequency coil, a human body phantom, and a highly detailed model of a pacemaker system with a bipolar lead.

Several configurations of pacemaker systems exposed to MRI are modeled and the results clearly show the importance of detailed lead modeling. Furthermore, modeling of resonant structures is investigated by a comparison between different modeling techniques.

Contents

1 Introduction

The three electromagnetic fields present in magnetic resonance imaging (MRI) all interact with passive and active medical implants. The static field can create forces and torques on the implant whereas the gradient fields, which are in the kHz-range, can cause vibrations, electrical interference and nerve stimulation. The radio frequency (RF) field can cause severe highly localized heating near sharp corners and edges of an implant. In particular, elongated conducting implants, like deep brain stimulation and pacemaker leads, can suffer from severe heating at their ends.

Currently, the number of MRI examinations per year is steadily increasing at the same time as medical implants are becoming an integral part of modern healthcare. Unfortunately, the interactions described above causes active implantable medical devices to be classified as a contraindication for MRI, i.e. a patient with such an implant is not allowed to undergo an MRI examination. Although there are two commercially available pacemaker systems which are conditionally safe in MRI [1, 2] and several MRI examinations have been performed on pacemaker patients without negative effects [3], the interactions between the electromagnetic fields and the pacemaker system during MRI is still an important topic to investigate. Especially as the available conditionally MR safe pacemaker systems are only approved for 1.5 T MRI scanners and have certain limitations (large parts of the torso can not be imaged with the system in reference [1] and the lead diameter is increased with respect to non MR approved leads with the system in reference [2]).

The electromagnetic fields generated by the RF coil of the MRI system induce currents in the body tissue and in the conductors of the implanted pacemaker lead. The lead constitutes a resonant structure and charge can be accumulated at its ends. Near the ends with accumulated charge, strong electric fields heat the conductive body tissue by Joule heating.

In order to further understand the factors influencing the heating, and ultimately to find a pacemaker lead design which is inherently safe in MRI, we model the electromagnetic part of the problem. First, we discuss the modeling challenges (section 2.1) and previous modeling efforts presented in the literature (section 2.2). Next, we present our modeling approach in section 2.3 and in section 2.4 the performance measures used in this study are described.

In the results section (section 3), we characterize the approximations in our modeling by investigating resonant structures in section 3.1. Finally, we devote section 3.2 to the investigation of pacemaker systems in MRI, a study based on the proposed model.

2 Modeling

2.1 Challenges

Modeling of pacemaker lead heating during MRI faces three major challenges which are described below.

2.1.1 Inter-examination variability

Several factors with strong impact on the lead heating show large variations between different patients and healthcare establishments. For example, the type of MRI machine and examination (RF field strength, imaging sequence, duration of the imaging procedure, body structure being imaged) vary between examinations. Furthermore, the patient position in the RF coil, the position of the pacemaker and lead configuration inside the patient, and patient characteristics (size, morphology, posture) are different for different examinations. In addition, variations exist in length and design of the pacemaker lead as well as in the type of implanted device. Thus, the number of different combinations of the factors mentioned above is vast wherefore individual simulations of each combination is an intractable approach.

2.1.2 Body tissue heterogeneity

The different tissue types present in the human body are both geometrically complex and differ strongly in dielectric properties. For example, Liu et al. [4] used conductivity values from 0.02 S/m (yellow marrow) to 2.3 S/m (cerebrospinal fluid) and values for the relative permittivity from 7 (fat and mammary tissue) to 128 (intestine/bowel content) in their simulations of an MRI system operating at 64 MHz. Volume discretizing computational methods, such as the finite element method (FEM) and the finite-difference time-domain method (FDTD), are normally preferred to boundary discretizing methods, such as the method of moments (MoM). This is due to the higher computational cost of MoM, when compared to the FEM and FDTD, for simulations that exploit highly detailed human body models.

2.1.3 Multi-scale problem

Several length scales are present in the problem. At 64 MHz, the wavelength λ_0 of the RF field in free space is roughly five meters. Thus, the human body has a size of approximately $\lambda_0/3$. Inside the body, the wavelength is reduced to $\lambda = \lambda_0/\sqrt{\varepsilon_r}$

where ε_r is the relative permittivity of the body tissue. Despite this reduction of the wavelength, some components of the pacemaker lead have dimensions on a length scale of approximately $\lambda/1000$. Volume discretizing methods are able to resolve these length scales concurrently but suffer from overwhelming simulation times and memory requirements.

2.2 Related work

Previously, Yeung et al. [5] used the MoM to model bare and insulated, straight wires in an infinite homogeneous lossy medium. They used this model to investigate the impact of the wire diameter, the insulation permittivity and thickness, and the tissue conductivity. The same authors also used this model in reference [6] to study the impact of the phase distribution of the external field. By changing this phase they constructed an excitation with maximal heating. The same type of modeling and ideas was elaborated on by Park et al. [7, 8] who developed a transfer function that relates the tangential part of the external field impingent on a small part of the lead with the electric field near the end of the lead. Different, more complex, lead designs were compared by Bottomley et al. [9] without resolving their finer details.

Modeling with detailed anatomical models based on the FDTD technique was performed by Pisa et al. [10] and Mattei et al. [11] where the latter valdiated the RF coil model against experiments. Furthermore, Vogel et al. [12] showed that the FEM can be used for lead heating simulations by modeling an entire examination room with an open MRI system. However, all these studies used simple lead models.

A more ambitious study was performed by Park et al. [13] who used 100 lead paths in each of 22 different human body models to compute the dissipated power at the lead tip using FDTD. Animal tests (dogs) were then performed where a lead was end-fed with RF-power of different levels and the corresponding change in pacing capture threshold (a significant marker for tissue heating) was measured. By combining the two populations of results, a probability curve could be generated which gave the probability for the entire range of changes in pacing capture threshold. Unfortunately, it is unclear how the leads were modeled.

The most detailed lead modeling available in the literature is presented by Neufeld et al. [14]. They used a two-step method with FDTD to fully resolve a single helix-shaped conductor. The results were then compared to measurements on the same lead and the difference between these results was shown to be within the uncertainty range through a sensitivity analysis.

However, modern pacing leads have geometries that are more complex than the one examined by Neufeld et al. In addition, experiments performed by Bottomley et al. [9] show that the finer details of the pacemaker lead strongly influence the heating around the lead tip. Therefore, we continue and extend our work presented in reference [15] and focus on pacemaker systems with a wide range of length scales modeled simultaneously. In particular, we use the MoM which discretizes boundaries between dielectrically different media. In order to keep the problem size within feasible limits, we simplify the complexity of the human body by modeling it as homogeneous according to the test standard ASTM F2182-09 [16]. Apart from the multi-scale modeling, this simplification has the additional advantage that it enables comparison of the results with results from controlled measurements. Such comparisons could prove difficult if highly detailed models, such as the Virtual Family [17], were used.

2.3 Proposed model

We aim at modeling the RF part of the ASTM test standard [16] which describes a lead heating experiment for cylindrical bore MRI systems. Here we consider such a system with a 1.5 T static magnetic field. The model contains an RF birdcage coil, an RF shield, a human body phantom, and an implanted pacemaker system consisting of a pacemaker unit and a bipolar lead. Each part of the model is explained in detail below. Our modeling environment is modularized to provide flexibility and it uses the frequency domain MoM available in the commercial software Efield® [18, 19].

2.3.1 RF birdcage coil

We model a generic RF birdcage coil consisting of two end rings connected by a variable number of equally distanced rungs. An example of a coil mesh is shown in figure 2.1. Both the end rings and the rungs are modeled by infinitely thin strips which are discretized with triangles. The entire coil is modeled with a perfect electric conductor (PEC) material. The coil is monochromatically excited at 64 MHz by a voltage source at the middle of each rung. All sources are assigned unit amplitude with a linear phase variation of 2π around the circumference of the coil. This models the currents that yield an RF field that is homogeneous in the center region of the coil, which is desired for MRI. Normally, real-life coils are fed only at two points on one of the end rings and the desired RF field with rotating magnetic field vector is obtained at the desired frequency by tuning capacitors. The feeding used in our model yields similar currents as with the real-life feeding but without having to tune any capacitors. Further information on different approaches for modeling birdcage coils can be found in reference [20], where the FDTD method was used.

2.3.2 RF shield

RF shields are used to shield the space outside the coil from the RF field and also to shield the RF coil from interactions with the surroundings since such interactions can have negative impact on the performance of the RF coil. We model the RF

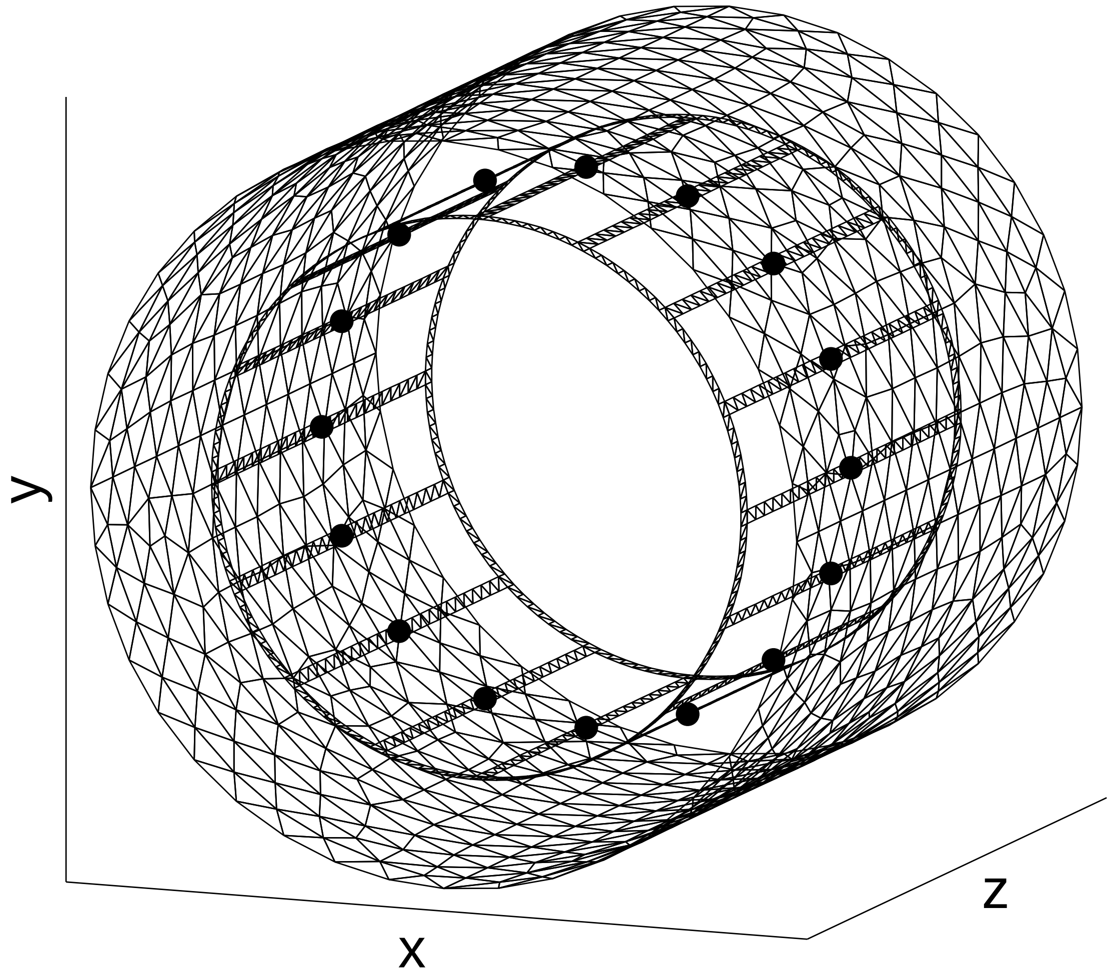

Figure 2.1. A 16-rung RF birdcage coil surrounded by an RF-shield. The source positions on the coil rungs are marked with black dots.

shield as a cylindrical shell sharing symmetry axis with the birdcage coil. The RF shield is assigned a PEC material in the model. An example of an RF shield mesh is shown in figure 2.1.

If the RF shield is placed close to the coil and extends beyond the ends of the coil, the image of the birdcage coil in the RF shield is in itself a birdcage coil with currents flowing in the opposite direction as compared to the currents on the original coil [21]. The field pattern inside the coil is therefore not significantly influenced by the presence of an RF shield. However, the field strength inside the coil is reduced due to the image currents. Depending on the purpose of the modeling and the type of model used for the birdcage coil, the RF shield can in many cases be excluded from the model without any major impact on the quantities of interest.

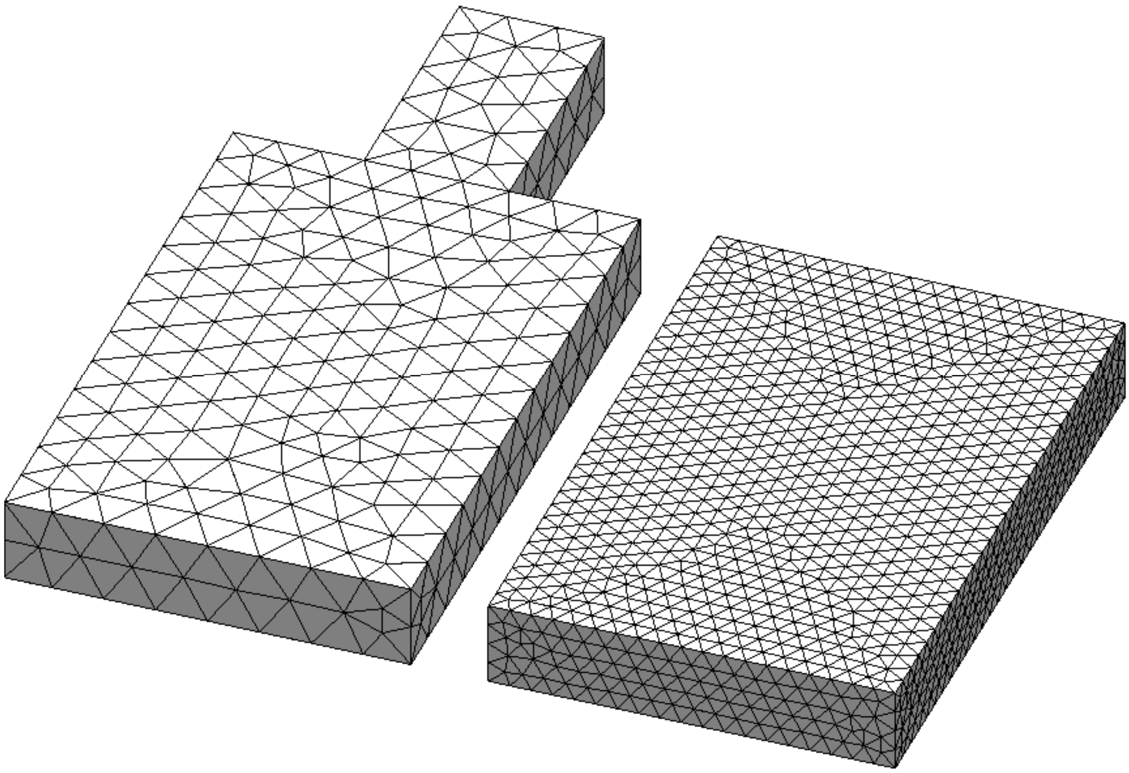

Figure 2.2. Surface meshes of two human body phantoms: with head and maximum element size of $\lambda/10$ (*left*), and without head and maximum element size of $\lambda/20$ (*right*).

2.3.3 Human body phantom

We use a homogeneous body phantom according to the ASTM test standard [16]. The phantom is shaped as a rectangular block filled with a lossy dielectric and it is intended to mimic the torso of an adult. The presence of a head on the phantom is optional. We use COMSOL Multiphysics [22] to create two models of the phantom, one with and one without the head. COMSOL is also used to mesh the phantoms' surfaces and to export the meshes to our simulation environment. Examples of these meshes are shown in figure 2.2.

2.3.4 Implant

We model a pacemaker system consisting of a pacemaker unit and a bipolar lead. The lead has two helix-shaped coaxial conductors: one inner conductor and one outer conductor which are modeled with straight segments using the MoM thin-wire approximation. In turn, each conductor consists of one or several filars, which are connected at each end of the lead but otherwise insulated from each other.

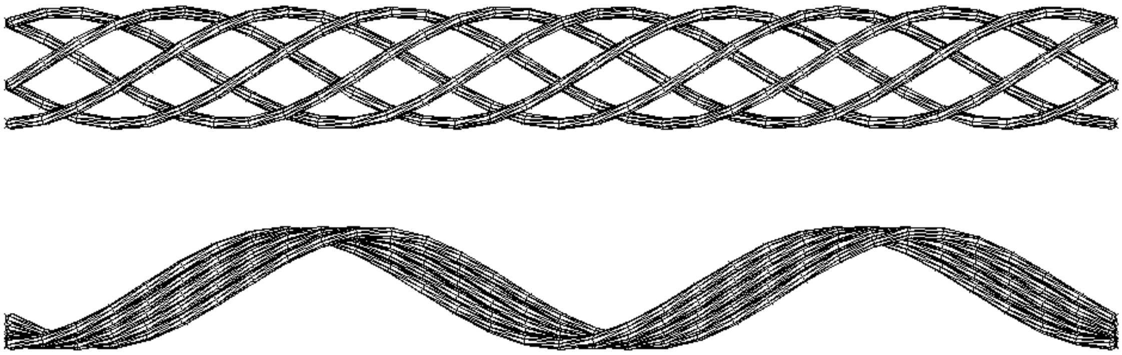

Figure 2.3. Equidistant (*top*) and tight (*bottom*) filar winding.

(Should the filars not be insulated from each other, a modeling approach based on a conducting strip instead of a set of wires could prove useful.)

In figure 2.3, two different filar windings are shown. In the upper part of the figure, the filars are equidistantly spread along the turn whereas they are tightly packed in the lower part of the figure, i.e. wound in such a way that the filars are almost touching. The conductors/filars are meshed using the area compensating scheme described in [15] which reduces the number of wire segments needed per turn for a certain discretization error. The conductors are fully enclosed in a tube of insulating dielectric.

The distal end of the lead, i.e the end of the lead which connects to the heart, features a tip electrode and a ring electrode that are modeled as PEC. This models a pacemaker lead with passive fixation where the tines have been left out. The inner conductor connects to the backside of the tip electrode whereas the outer conductor connects to the backside of the ring electrode. The boundary conditions assigned to the electrode surfaces impose a purely tangential current which means that current can not enter nor exit the lead at these electrodes. This model is a simplification of the corresponding physical situation that is far more complex, see for example reference [23] for more details on the contact impedance and related matters. Figure 2.4 shows a mesh of the distal end of the lead together with a photo of a clinical pacemaker lead.

The path followed by the lead in space, or the lead configuration, is described by a parametric curve $\Gamma : (x(s), y(s), z(s)), s \in [0, 1]$. The surface elements of the insulation and the two electrodes are generated as follows. At the start ($s = 0$), a local coordinate system $(\vec{u}, \vec{v}, \vec{w})$ is chosen such that $\vec{w}$ is parallel to the tangent of the lead path. A number of points are placed evenly on a circle in the uv-plane before a step is taken along Γ by letting $s = \delta s$. Once again the tangent vector along Γ is set as $\vec{w}_{s=\delta s}$. The basis vector $\vec{u}_{s=\delta s}$ is now obtained as the part of $\vec{u}_{s=0}$ which is orthogonal to $\vec{w}_{s=\delta s}$. The same number of points as before are now placed evenly on a circle in the uv-plane. Triangular elements are created using these two rings of points. The procedure continues similarly until the end of the lead $s = 1$. Thus, a tubular shell is obtained. The shell can be closed at the ends by inserting a point at

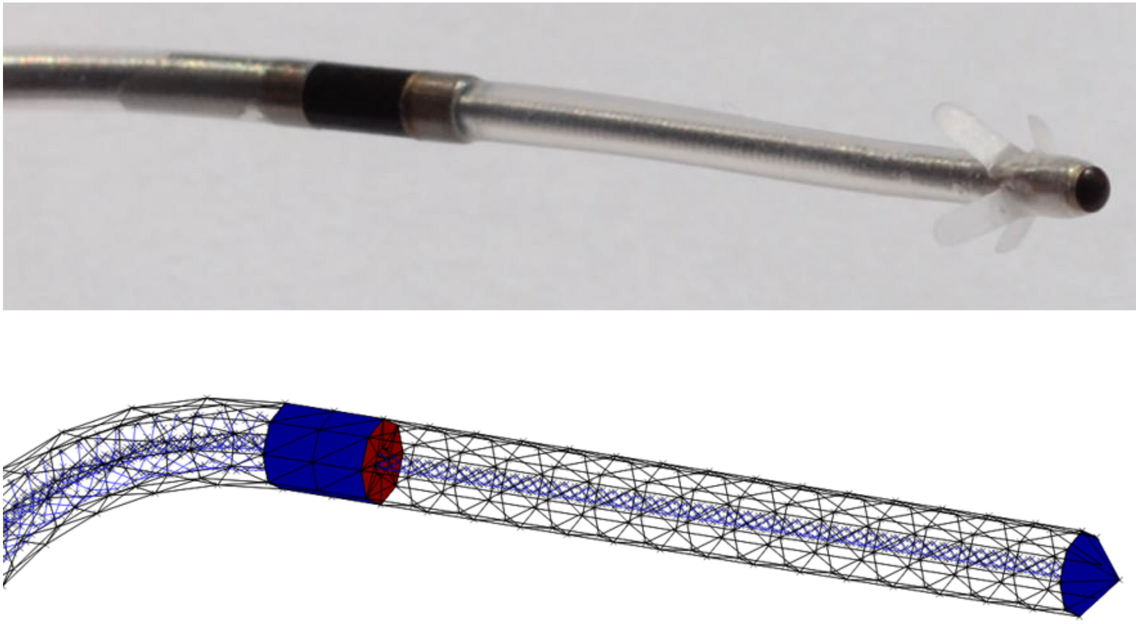

Figure 2.4. Photo of a clinical pacemaker lead (*top*) and a mesh of the same part of the lead (*bottom*).

the origin of the first/last local coordinate system and adding triangles between this midpoint and the points on the boundary of the tubular shell. The midpoint can also be displaced a small distance in the $(-w/+w)$-direction to generate a pointed tube. Note that it is important to reuse $\vec{u}_{s=s_1}$ when generating $\vec{u}_{s=s_1+\delta s}$ in order to save the tube from twisting, which could render the mesh useless.

The wire segments of the conductors are created using the same approach as above with local coordinates. The difference is that at each s only one point is added on the circle in the uv-plane. The angle between the point and $\vec{u}$ is a linear function of s which generates a helix when the points corresponding to two neighboring values of s are connected with a line segment.

A pacemaker unit is placed at the other end of the lead compared to the electrodes. The pacemaker unit is modeled as a hollow rectangular box made of PEC material filled with insulation. The pacemaker measures 6 cm $\times$ 6 cm $\times$ 1 cm and it is meshed using COMSOL with a maximum element size of $\lambda/50$. The conductors enters through a circular hole in the pacemaker. Inside the pacemaker, the inner conductor is connected to the outer one through a lumped component which models the electronics of the pacemaker unit. The outer conductor is also connected to the metal shell of the pacemaker unit through a lumped component. A mesh of a pacemaker lead with an attached pacemaker unit is shown in figure 2.5.

Simulations without the pacemaker unit can also be performed. In this case, the lead ends with the two conductors being connected through a lumped component, where the termination of the two conductors and the lumped component are embedded in

Figure 2.5. Mesh of a pacemaker lead with an attached pacemaker unit.

the insulation of the lead.

2.3.5 Standard model setup

The parameter values stated below are used throughout this work unless stated otherwise.

RF birdcage coil The standard model setup uses a birdcage coil modeled with patches and parameters according to table 2.1. The birdcage coil operates at 64 MHz and is excited as described in section 2.3.1.

Parameter	Value
Number of rungs	16
Rung width	6.5 mm
Cage radius	0.3 m
Cage length	0.6 m
Maximum element size	0.01 m

Table 2.1. Parameter values for the standard setup of the birdcage coil.

RF shield Since our model of the birdcage coil does not include tuning capacitors and the fields are scaled to obtain a specified specific absorption rate (SAR) level in the phantom, the RF shield has no impact on the simulation results (see section 2.3.2). It is therefore excluded from the standard setup.

Human body phantom The standard model setup uses the head-less human body phantom described in the test standard [16] with parameters according to table 2.2.

Implant The standard model setup uses an insulated bipolar pacemaker lead inserted into the human body phantom. The electrical conductors of the lead are modeled using the thin-wire approximation. The corresponding parameters are listed in table 2.3.

Parameter	Value
Height	0.65 m
Width	0.42 m
Depth	0.09 m
Relative electric permittivity, ε_r	80
Relative magnetic permeability, μ_r	1
Electric conductivity, σ	0.5 S/m
Position in RF coil	Centered
Maximum element size	$\lambda/20$

Table 2.2. Parameter values for the standard setup of the human body phantom.

2.4 Performance measures

The test standard ASTM F2182-09 [16] uses two performance measures: the local SAR and the local additional temperature rise with the implant in place. The SAR is defined by

$$\mathrm{SAR} = \frac{1}{2}\int_{\Omega} \frac{\sigma(\vec{r})|\mathbf{E}(\vec{r})|^2}{\rho(\vec{r})}\, d\Omega \tag{2.1}$$

where σ is the electric conductivity of the tissue, $\mathbf{E}$ is the electric field phasor, ρ is the density of the tissue, $\vec{r}$ is the position vector, and Ω the region of tissue over which the quantities are averaged. These two performance measures are also common in previous modeling, for example Neufeld et al. [14] and Yeung et al. [24]. In order to model the temperature rise, a heat problem must be solved where the result of the electromagnetic simulation is used as source term. However, we are, at least in a first step, interested in relative instead of absolute performance measures since our aim is to compare the heating performance of different lead designs. In addition, the heat equation has a smoothing effect on the distribution of the source term, see for example [24], wherefore we use different electromagnetic quantities as performance measures instead.

At least three different performance measures can be used:

- **Electric field around implant electrodes**
  The tissue is heated by Joule heating. These power losses, and the corresponding source term in the heat equation, are proportional to the square of the absolute value of the electric field. This measure is very closely related to the SAR, as defined in equation (2.1), with the advantage of not having to decide over which mass of tissue the quantity should be averaged.

- **Accumulated charge on the electrode surfaces**
  The electric field in the electrode vicinity is proportional to the accumulation of charge on the electrode surfaces.

- **Maximum value of the induced current**
  The accumulation of charge at the ends of the lead is associated with currents

Parameter	Value
Impedance between inner and outer conductors	
at PM end	$0\,\Omega$, (i.e. short circuit)
Number or conductors	2
Helix diameter, from center of wire	$(0.58, 1.3)$ mm
Wire diameter	$(0.1, 0.1)$ mm
Number of conductor filars	$(1, 1)$
Filament spacing	N/A
Helix length (excluding the part from tip to ring)	500 mm
Helix pitch height	$(0.84, 0.675)$ mm
Helix winding	(Right,Right)
Wire segments per helix turn	$(6, 6)$
Use meshing with area compensation	Yes
Implant configuration	Straight
$x(s)$	$0 * s$
$y(s)$	$0 * s$
$z(s)$	$1 * s$
Implant position (backside of ring)	
x_0	0.17 m
y_0	0 m
z_0	-0.25 m
Insulation	
Outer diameter	2 mm
Expand diameter through area compensation	Yes
Element size along lead	2 mm
Number of elements around lead circumference	6
Relative electric permittivity, ε_r	3
Relative magnetic permeability, μ_r	1
Electric conductivity, σ	0 S/m
Tip and ring	
Ring, length	2.5 mm
Ring, inner diameter	0.796 mm
Distance between ring and tip	12 mm
Number of elements around lead circumference	6
Maximum element height	1 mm
Pacemaker present	No

Table 2.3. Parameter values for the standard setup of the implant. If two values are listed they should be read as (value for inner conductor, value for outer conductor).

induced in the lead by the tangential component of the external field. An increase in tissue heating is due to stronger electric fields and currents in the tissue. The increase of these fields and currents is associated with increases in accumulated charge and induced currents on the lead.

3 Results

3.1 Modeling of resonant structures based on the thin-wire approximation

The conducting wires in pacemaker leads are normally shaped as helices. The helix length is comparable to the wavelength of the RF field in the human body but the helix diameter is far smaller than the wavelength. Below, we therefore investigate the electromagnetic properties of helices and especially the impact of the helix pitch angle. We also study the validity of the thin-wire approximation when applied to modeling of helices.

3.1.1 Single helix

Comparison with surface discretization

In order to investigate the validity of the thin-wire approximation when modeling resonant structures, such as a pacemaker lead, we model a single helix in free space excited by a plane wave. The plane wave is polarized along the helix axis and it impinges on the helix perpendicularly to this axis. A frequency interval corresponding to $L_{\text{wire}}/\lambda \in [0.1, 6.1]$ is studied where L_{wire} is the total wire length.

The helix has the following characteristics: 90 turns, wire diameter d, outside helix diameter $11d$ and pitch height $1.1d$ which corresponds to a pitch angle $\Psi = 2.0°$ and an inter-turn distance of $0.1d$. That is, the turns are almost in contact with each other. The wire and helix diameters are both significantly shorter ($< 2.4\%$) than the wavelength of the plane wave at the highest frequency.

The problem is solved using the thin-wire approximation as well as using a standard MoM approach where the surface of the wire is discretized. To assure a fair comparison between the results, one thin-wire segment models the same part of the helix wire as a straight cylinder does in the surface discretization. The surface discretization is expected to give a more accurate result since it permits current distributions that are not constant around the circumference of the wire as assumed by the thin-wire approximation. In addition, it can model currents flowing in the circumferential direction of the wire. A part of the geometry is shown in figure 3.1 for the two different representations.

The maximum absolute value of the induced current is shown in figure 3.2 as a function of the total wire length normalized by the wavelength over a frequency band. Clearly, the resonant frequencies obtained with the thin-wire approximation

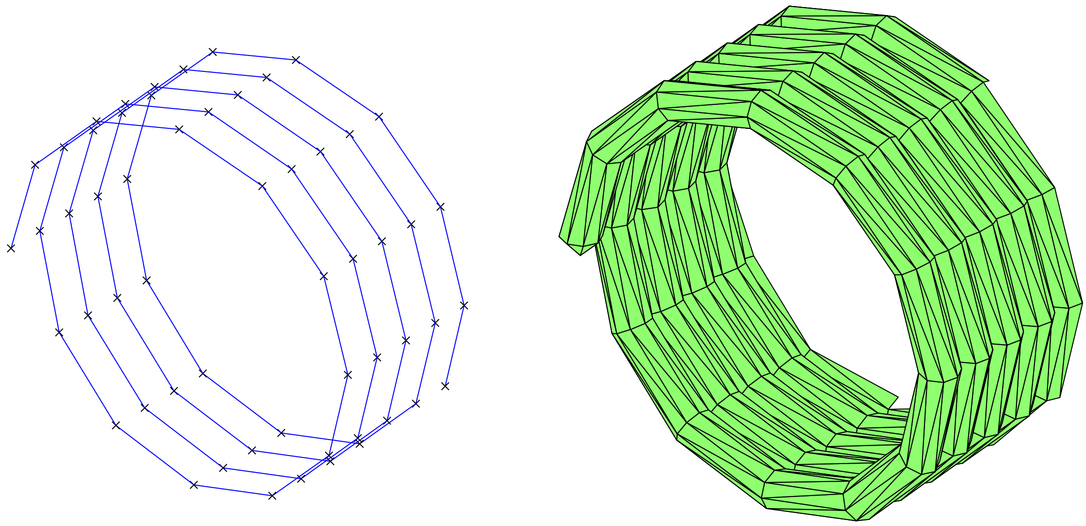

Figure 3.1. Thin-wire representation (*left*) and surface representation (*right*) of a couple of turns of the single helix.

are shifted to higher frequencies compared to their counterparts from the surface discretization. However, the overall current amplitude is very similar between the two modeling techniques. Similar simulations suggest that the difference in resonance frequencies decreases when the pitch angle increases. For example, the relative error in amplitude is smaller than 6% at the first resonance for $\Psi = 17°$.

Impact of helix pitch angle

A helix is defined by four geometrical parameters: the helix length, the pitch angle Ψ, the wire diameter, and the helix diameter. The helix length can also be described by the number of helix turns or the total wire length L_{wire}. Likewise, the pitch angle can be replaced by the pitch height in the description of the helix.

We investigate the impact of the pitch angle on the resonant frequencies of the helix by exploiting the same model as above at $\Psi = 2°$. The pitch angle is then increased in two different ways:

1. L_{wire} is kept constant. As a consequence, the number of helix turns and the helix length change when the pitch angle is varied.

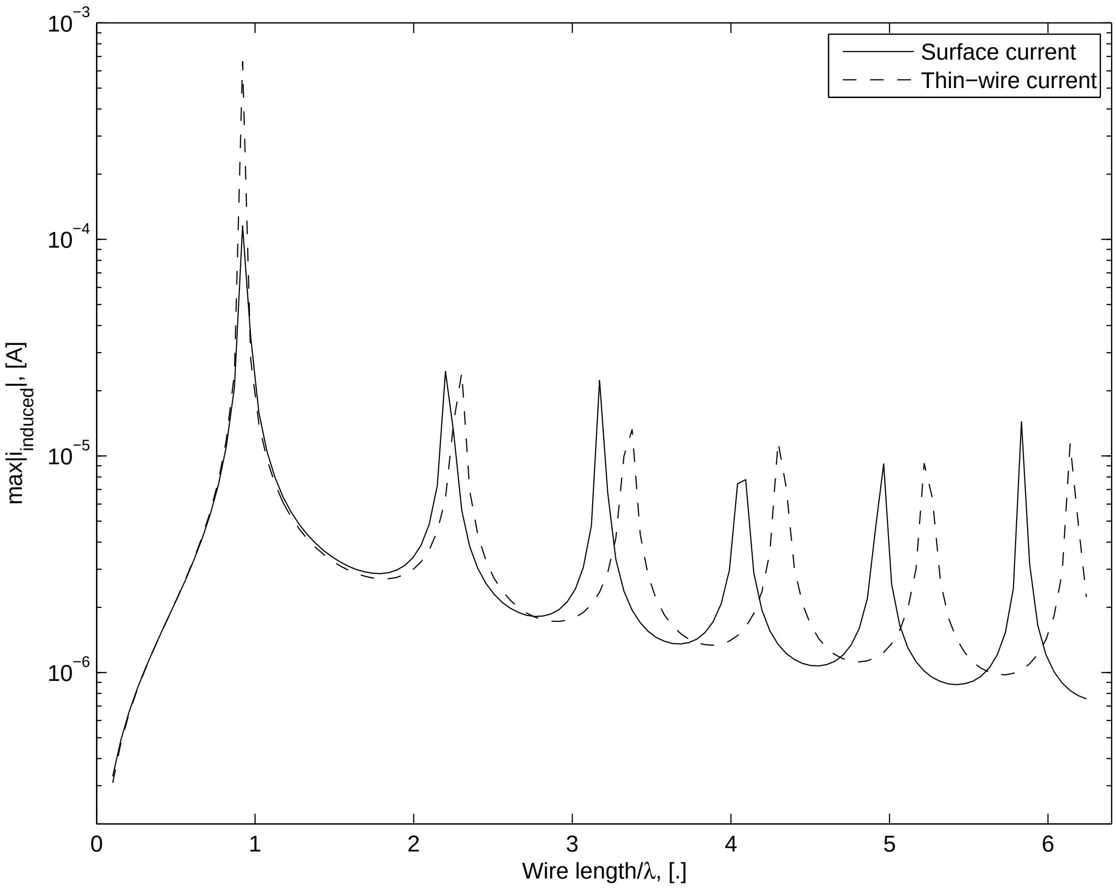

Figure 3.2. Maximum amplitude of the induced current obtained with thin-wire and surface modeling vs. normalized wire length at a helix pitch angle of $\Psi = 2°$. Note that the wire length has been scaled with respect to the wavelength, λ, of the incoming plane wave.

2. The number of turns is kept constant and, therefore, L_{wire} and the helix length change when the pitch angle is varied.

The wire and helix diameters are constant (and identical) in both cases. The helix is modeled using the thin-wire approximation.

Figure 3.3 shows the maximum amplitude of the induced current on the helix as a function of the pitch angle and the frequency of the incoming field for the case where L_{wire} is kept constant. Note that the frequency is expressed as the total wire length divided by the wavelength λ and that the current scale is logarithmic. In the limit $\Psi \to 90°$, the obtained results agree well with the standard results for dipole antennas where resonances occur at $L_{\text{wire}} = (n + \frac{1}{2})\lambda, n = 0, 1, 2, \ldots$.

When the pitch angle decreases, the resonances shift to higher frequencies. Furthermore, they also get more distantly spaced in frequency until the pitch angle reaches 10°. Below this angle, the resonances quickly move to lower frequencies and approach each other.

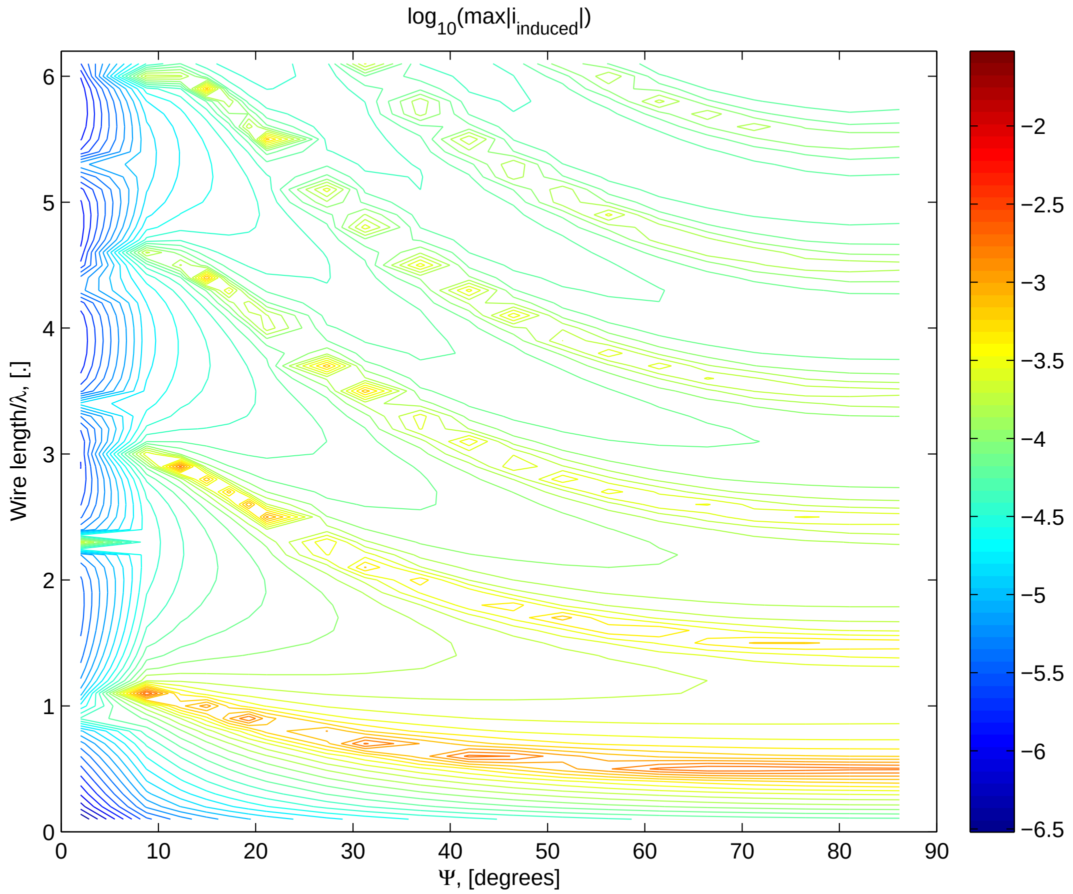

Figure 3.3. Maximum amplitude of the induced current vs. normalized wire length and helix pitch angle Ψ. The wire length is constant for all pitch angles but the number of turns and helix length changes. Note that the wire length has been scaled with respect to the wavelength, λ, of the incoming plane wave and that the current scale is logarithmic.

The corresponding results for the case where the number of turns is kept constant are shown in figure 3.4. The overall behavior is similar to the first case. However, it can be noted that the induced currents are stronger in the limit $\Psi \to 90°$ for this second case. Furthermore, the decrease in resonant frequencies for $\Psi < 10°$ can be more clearly seen for the second case than for the first case.

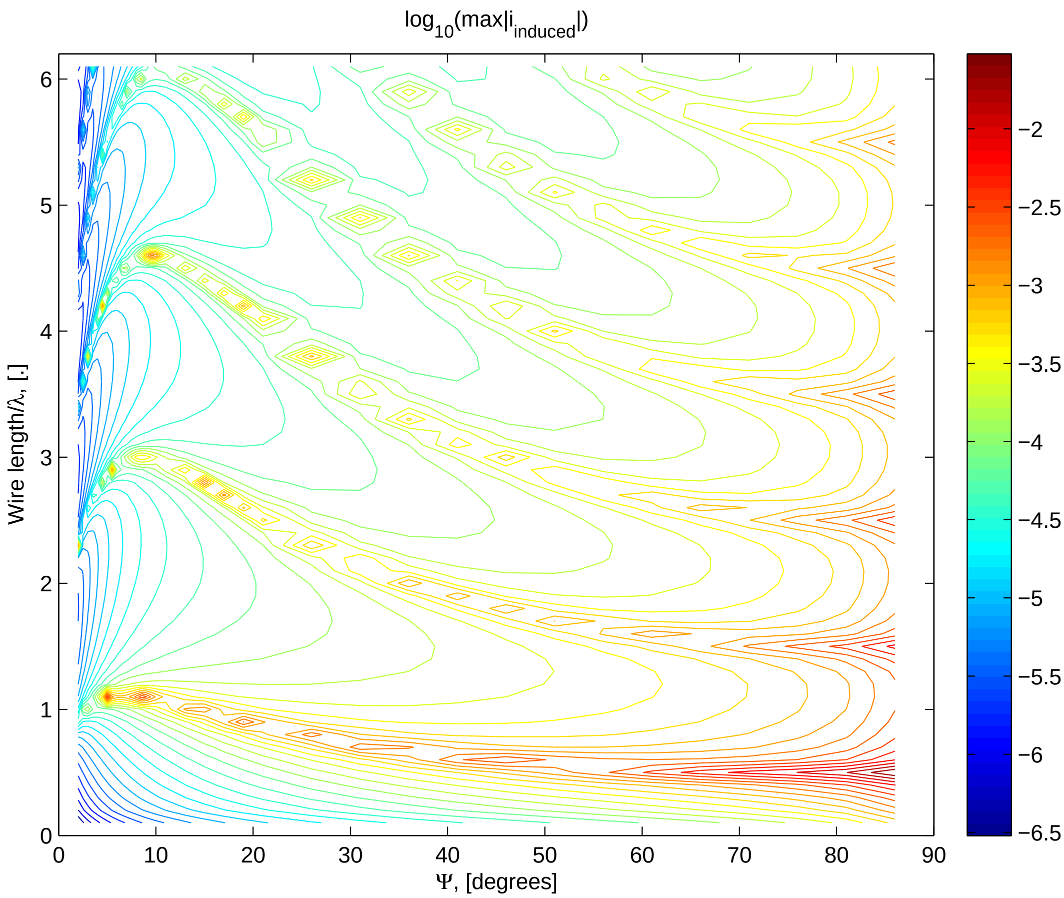

Figure 3.4. Maximum amplitude of the induced current vs. normalized wire length and helix pitch angle Ψ. The number of turns is constant for all pitch angles but helix and wire lengths change. Note that the wire length has been scaled with respect to the wavelength, λ, of the incoming plane wave and that the current scale is logarithmic.

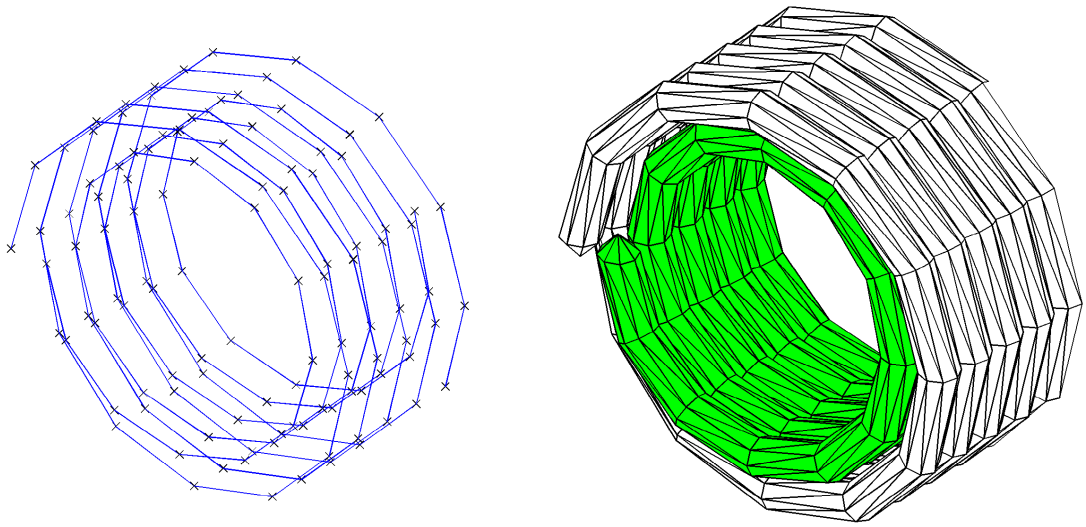

Figure 3.5. Thin-wire representation (*left*) and surface representation (*right*) of a couple of turns of the double helix with conductors wound in opposite directions.

3.1.2 Double helix

Comparison with surface discretization

The problem in section 3.1.1 is extended to include a second helix inside the first one. The outer helix is identical to the previous problem: 90 turns, wire diameter d, outside helix diameter $11d$ and pitch height $1.1d$ which corresponds to $\Psi = 2.0°$ and an inter-turn distance of $0.1d$. The inner helix shares helix length and pitch height with the outer, and has a wire diameter of d, an outside helix diameter of $8.8d$ and thereby $\Psi = 2.5°$. The distance between the turns of the inner helix as well as between the turns of the inner and outer helix is therefore $0.1d$. Thus, the setting corresponds to a very closely packed double helix without electrical contact between the wires, which should constitute a worst case for the thin-wire approximation. A part of the geometry with conductors wound in opposite directions is shown in figure 3.5 for the two different representations.

The maximum absolute value of the induced currents is shown in figure 3.6 for a double helix where both conductors are wound in the same direction. The currents on the inner and outer conductor behave similarly although slightly larger values

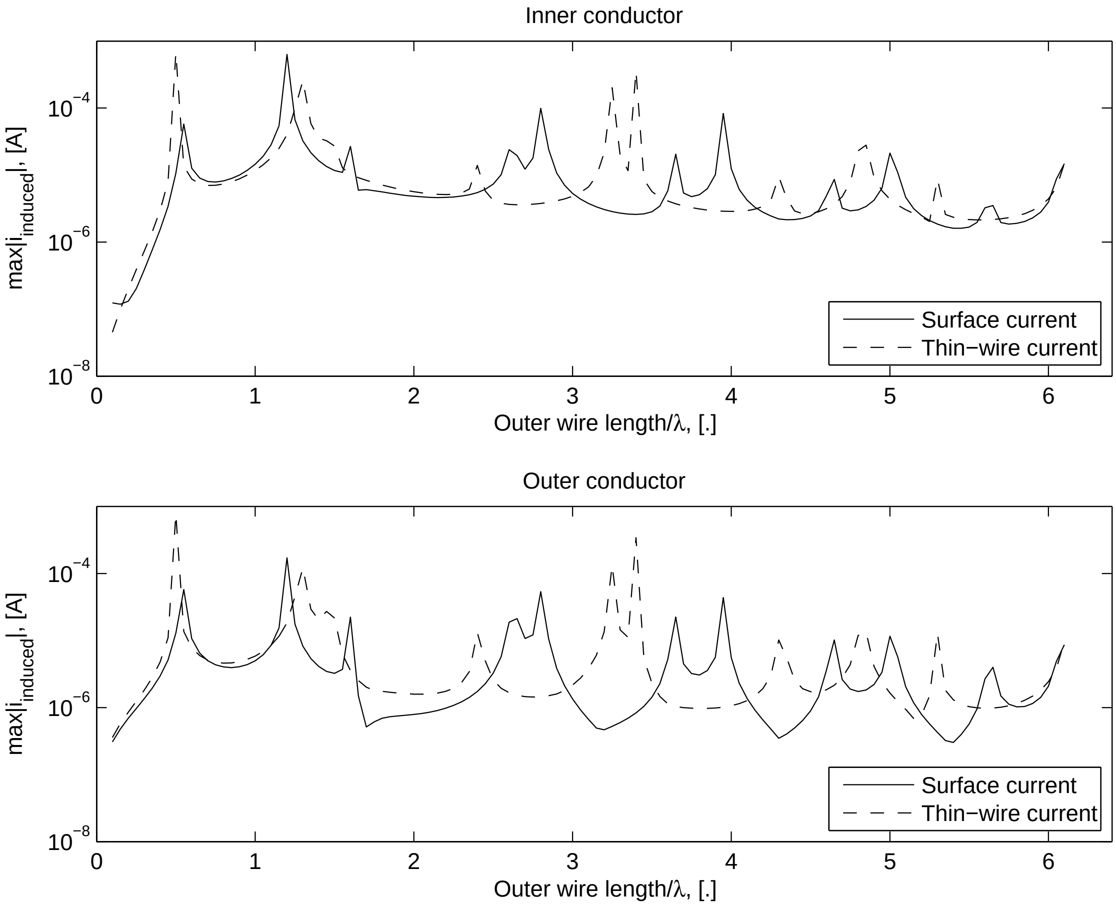

Figure 3.6. Maximum amplitude of the induced current obtained with thin-wire and surface modeling vs. normalized wire length for the inner (*top*) and outer (*bottom*) conductors of a double helix where the two conductors are wound in the same direction.

are taken by the current on the inner one. Furthermore, the number of resonant frequencies and their positions differ in the thin-wire results when compared to the surface discretization.

Similar results are shown in figure 3.7 where the conductors are wound in opposite directions. Although the overall shape of the curves change dramatically, the currents on the inner and outer conductor behave similarly. The differences remain between the thin-wire results and the surface results in terms of the number of resonances and their frequencies. In contrast to the single-helix results in section 3.1.1, the resonances given by the thin-wire approximation occur at lower frequencies than their counterparts obtained with the surface representation.

Even though the results obtained with the thin-wire approximation differ substantially from the surface representation results, the thin-wire approximation captures the general differences caused by the conductor winding scheme. When modeling based on the thin-wire approximation is employed in situations comparable to the

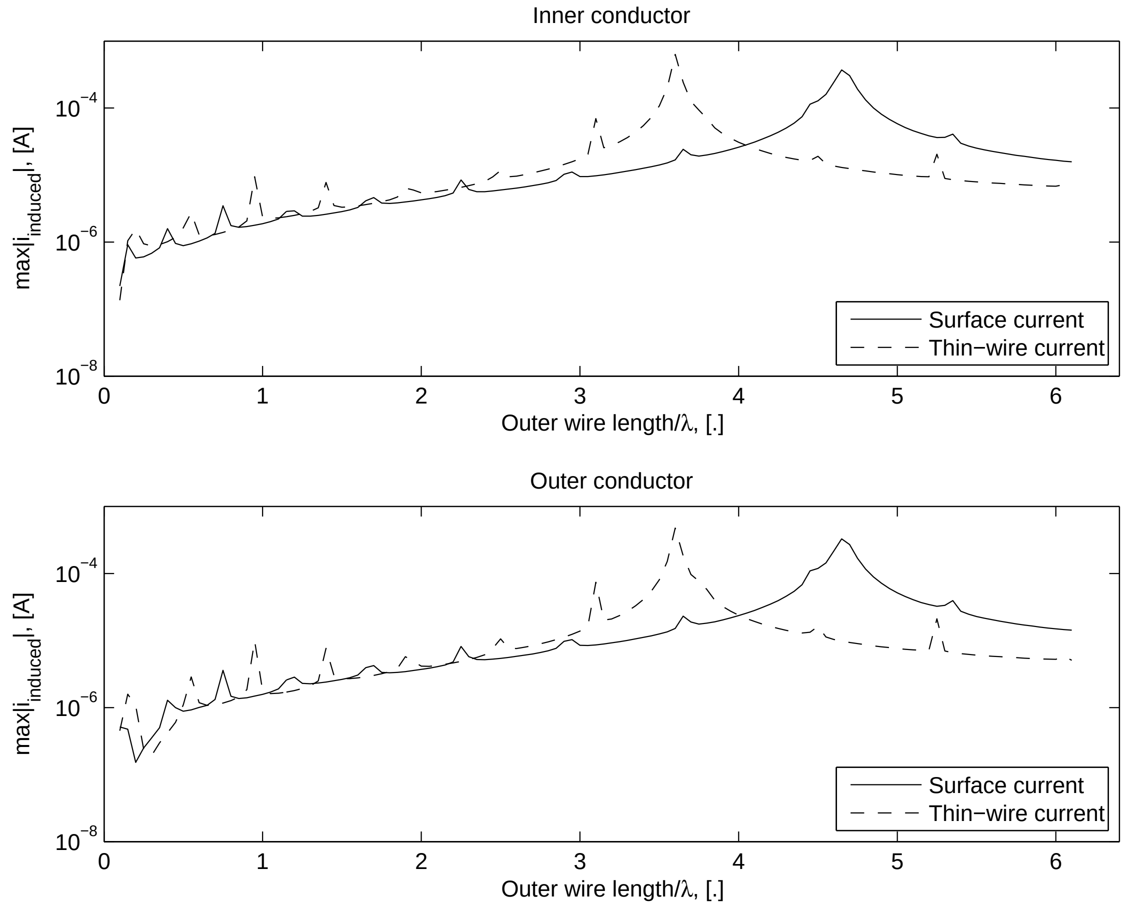

Figure 3.7. Maximum amplitude of the induced current obtained with thin-wire and surface modeling vs. normalized wire length for the inner (*top*) and outer (*bottom*) conductors of a double helix where the two conductors are wound in opposite directions.

situations presented above, an analysis over a frequency interval might provide information on the average level of the induced currents.

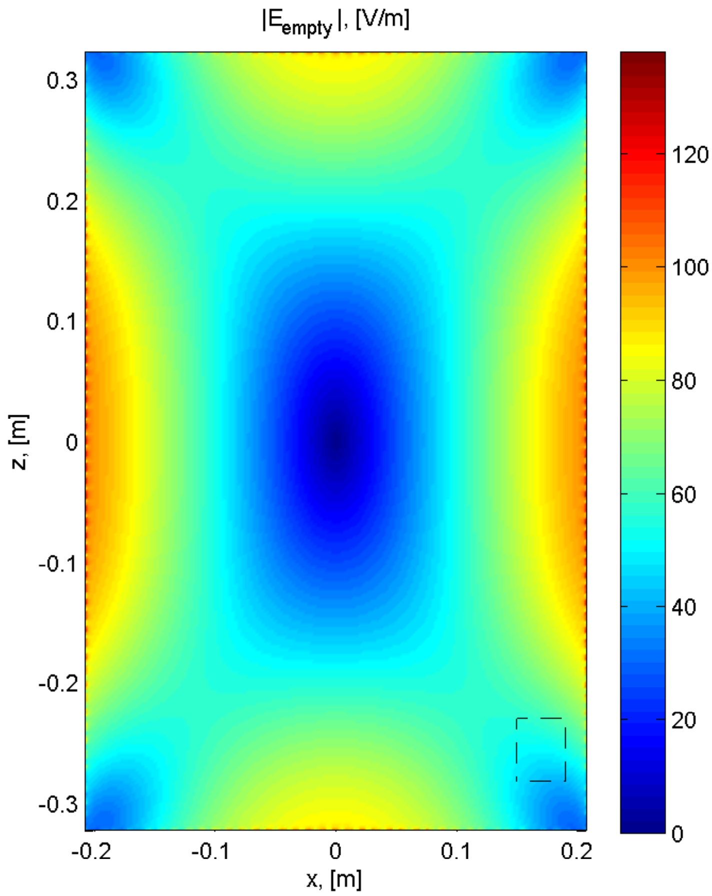

Figure 3.8. Absolute value of the electric field in an empty phantom for $y = 0$, i.e. through the middle of the phantom, for a whole-body averaged SAR of 1 W/kg. The dashed rectangle shows the area where the distal end of a pacemaker lead will be placed.

3.2 Modeling of pacemaker systems in MRI

Below, all results from simulations involving the MRI setup have been scaled to a whole-body averaged SAR of 1 W/kg by assuming that the body phantom is filled with a substance with the same density as water, $\rho = 1000\,\mathrm{kg/m^3}$.

The absolute value of the electric field in an empty human body phantom is shown in figure 3.8 in the plane $y = 0$. The electric field attains its highest values near the long edges of the phantom where the field is directed parallel to the edge. In order for the incoming electric field tangential to the lead to be as strong as possible, the ASTM test standard [16] dictates that the lead should be placed in a straight configuration close to, and parallel to one of the long edges of the phantom. The values shown in the figure will be used as reference throughout the following sections.

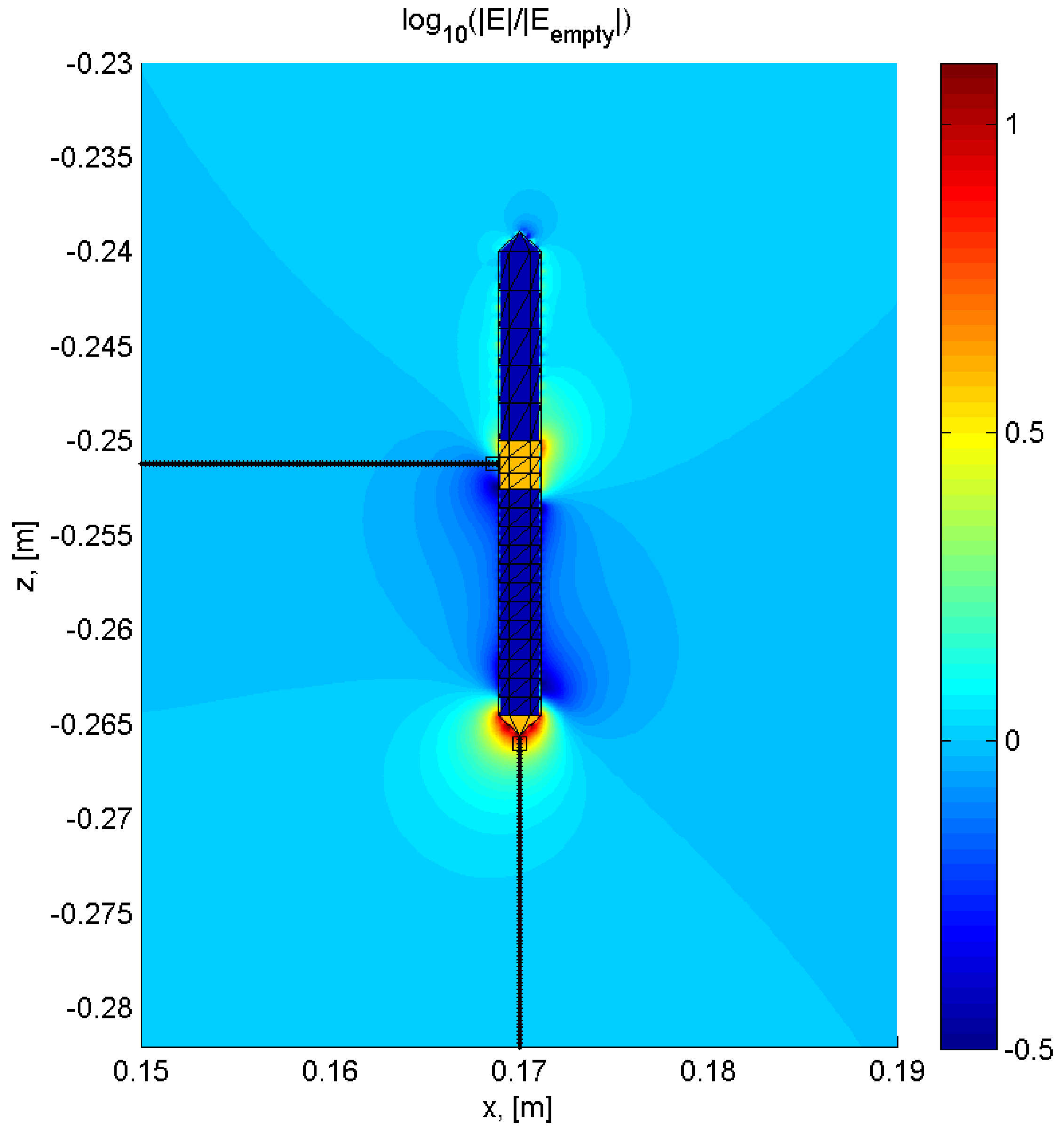

Figure 3.9. Amplification of the local electric field in logarithmic scale with a 1 cm lead in place, with respect to the case with an empty phantom.

3.2.1 Impact of lead length

We use the standard setup as described in table 2.3 and vary the lead length L from 1 cm to 55 cm in steps of 2 cm.

Figure 3.9 shows the ratio between the electric field amplitude with a 1 cm lead in place and the empty case. The same quantity is shown in figure 3.10 for a 55 cm lead. For the shorter lead, the local electric field is amplified by a factor of ten close to the tip and ring electrodes. In contrast, the amplification is predominant close to the tip electrode for the long lead where it reaches a factor larger than 200.

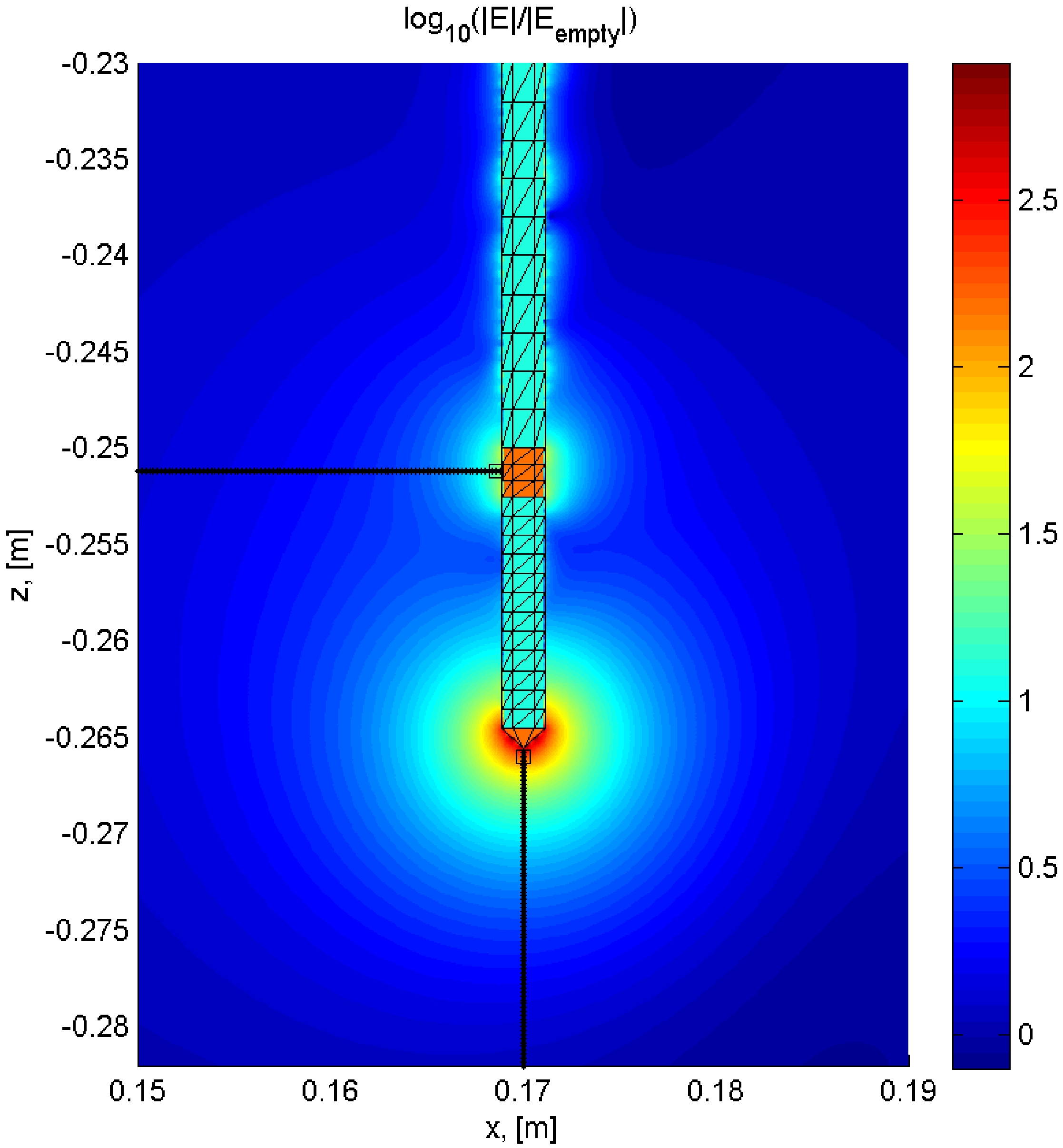

Figure 3.10. Amplification of the local electric field in logarithmic scale with a 55 cm lead in place, with respect to the case with an empty phantom.

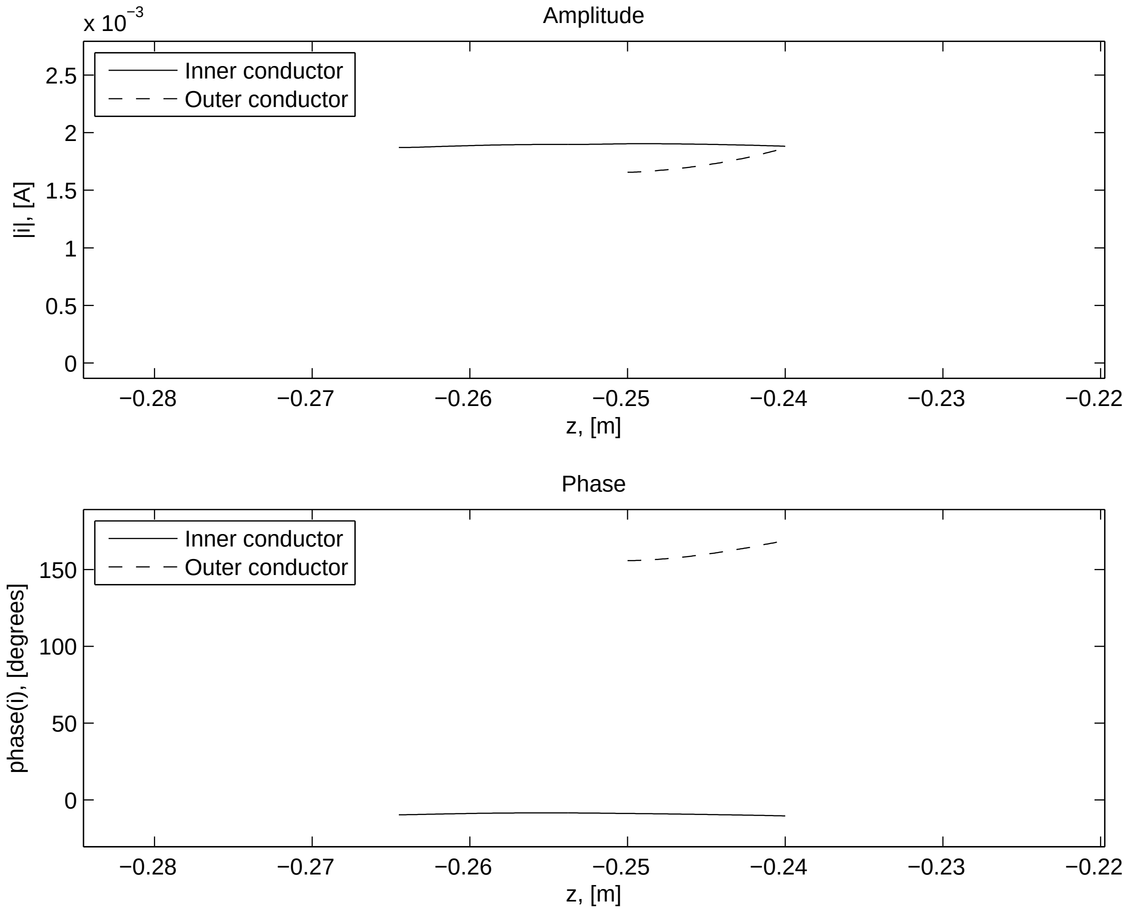

Figure 3.11. Amplitude (*top*) and phase (*bottom*) of the currents induced in a 1 cm lead as a function of z.

The induced currents on the lead conductors are shown in figure 3.11 for the shorter lead and figure 3.12 for the longer lead. The amplitude of the currents in the left-most part of the figures explains the different heating patterns seen previously. For the shorter lead, the currents entering the tip and ring electrodes through the inner and outer conductors respectively are of nearly equal size. The total charge on the electrodes will thereby be of similar size wherefore the amplification of the electric field is of similar value near the electrodes. Conversely, for the longer lead the current flowing on the inner conductor to the tip electrode is much greater than the current flowing on the outer conductor to the ring electrode. Consequently, the highest values of the electric field amplification are seen around the tip electrode. Furthermore, the amplitude of the current flowing to the tip electrode in the longer lead is about 50 times larger than the same current in the shorter lead. This is also reflected in the difference in amplification factor between the two leads.

Consider the shorter lead and figure 3.11. Note that the wire segment normals all have a z-component in the same direction. The almost equal amplitude values on the two conductors in combination with the phase difference of approximately 180° show that the charge oscillates between the two electrodes. The same effect is not

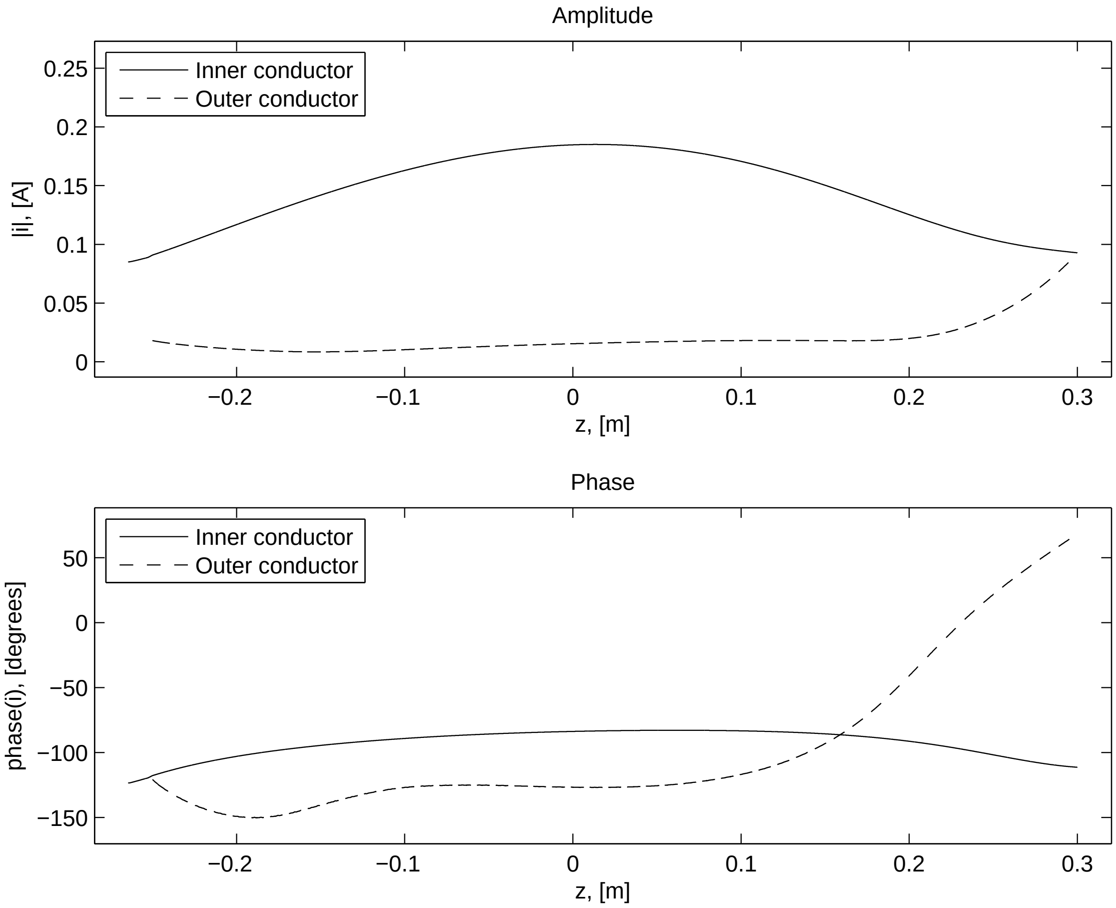

Figure 3.12. Amplitude (*top*) and phase (*bottom*) of the currents induced in a 55 cm lead as a function of z.

visible for the longer lead in figure 3.12. For this lead, charge accumulates on the tip electrode and is spread along the inner conductor. Very little charge sits on the outer conductor. (Note that from the law of conservation of charge, the amplitude of the charge is proportional to the derivative of the current with respect to z.)

In figures 3.9 and 3.10, two lines with points have been marked with dots. One line runs from the tip of the tip electrode in the same direction as the lead is oriented and the other line runs from the middle of the ring electrode perpendicularly to the lead. The amplitude of the electric field is evaluated at these points and it is shown in figure 3.13 for the line close to the tip and figure 3.14 for the line starting at the ring electrode. The lead length corresponding to these values is $L = 45\,\text{cm}$.

As expected, the electric field decays quickly with increased distance, r, to the electrodes. For the ring electrode, $r = 0$ corresponds to the symmetry axis of the lead. For the tip electrode, $r = 0$ corresponds to the midpoint of the base of the tip electrode polyhedron. The electric field near the tip decays as r^{-2} and the field near the ring a bit steeper than r^{-1}. This can be compared to the field from a point charge which decays as r^{-2} and the field from a line charge which decays as r^{-1}.

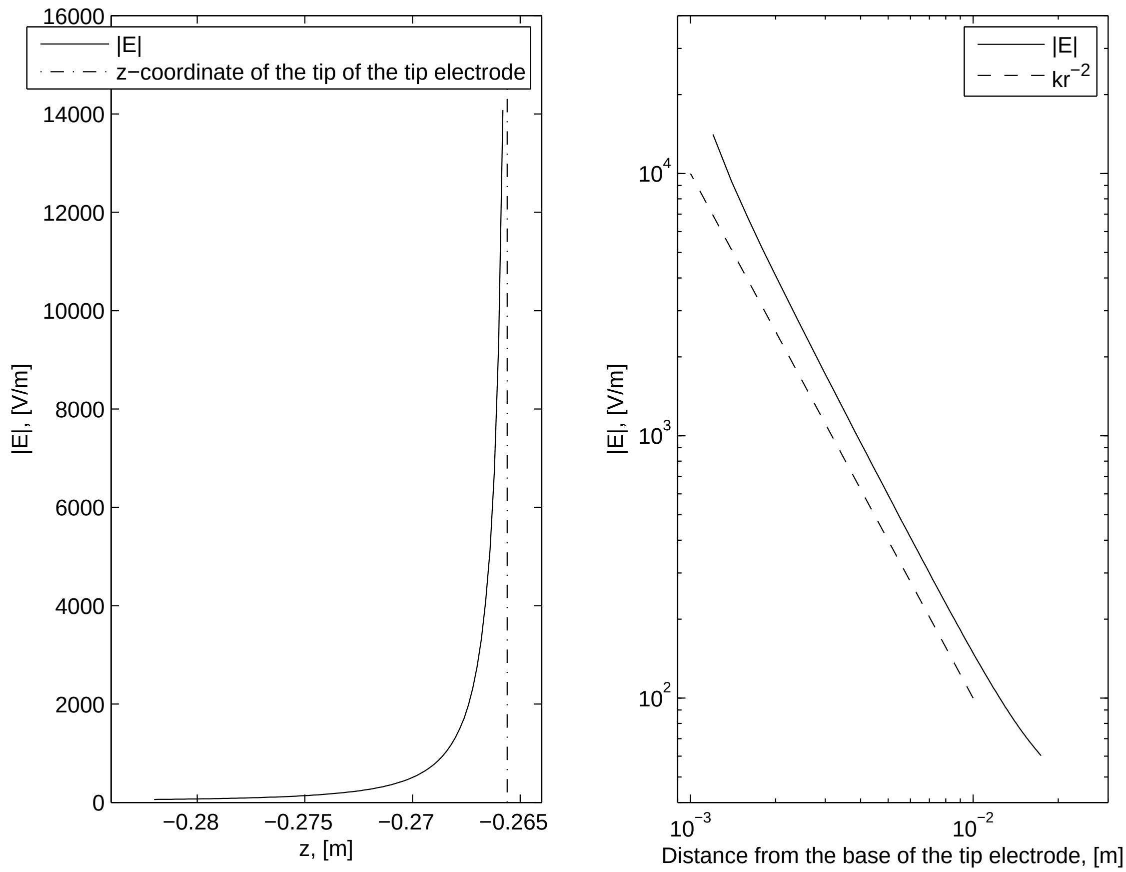

Figure 3.13. Amplitude of the electric field on a straight line from the tip electrode as a function of z (*left*) and distance from the tip base point (*right*). In the right hand plot, a function proportional to r^{-2} has been added for comparison.

Two points are marked with squares in figures 3.9 and 3.10. One is situated close to the tip and one close to the ring. The electric field is evaluated in these points for all leads of different length and the corresponding values are shown in figure 3.15. The electric field close to the tip increases with the lead length up to $L = 47\,\text{cm}$ from where it starts to decrease slightly whereas the electric field close to ring electrode reaches its highest value at $L = 43\,\text{cm}$. For maximum heating at the tip, the lead has a total length of 48.5 cm where the additional 1.5 cm is the distance fom the back of the ring to the tip. This length should be compared to the wavelength in the phantom tissue which is approximatly 52 cm. The electric field close to the ring electrode is weaker than the field close to the tip as has been seen above. This is due to a weaker current being induced in the outer conductor than in the inner conductor which has been shown previously in reference [15] for unconnected double helices in a similar setting, albeit at larger pitch angles.

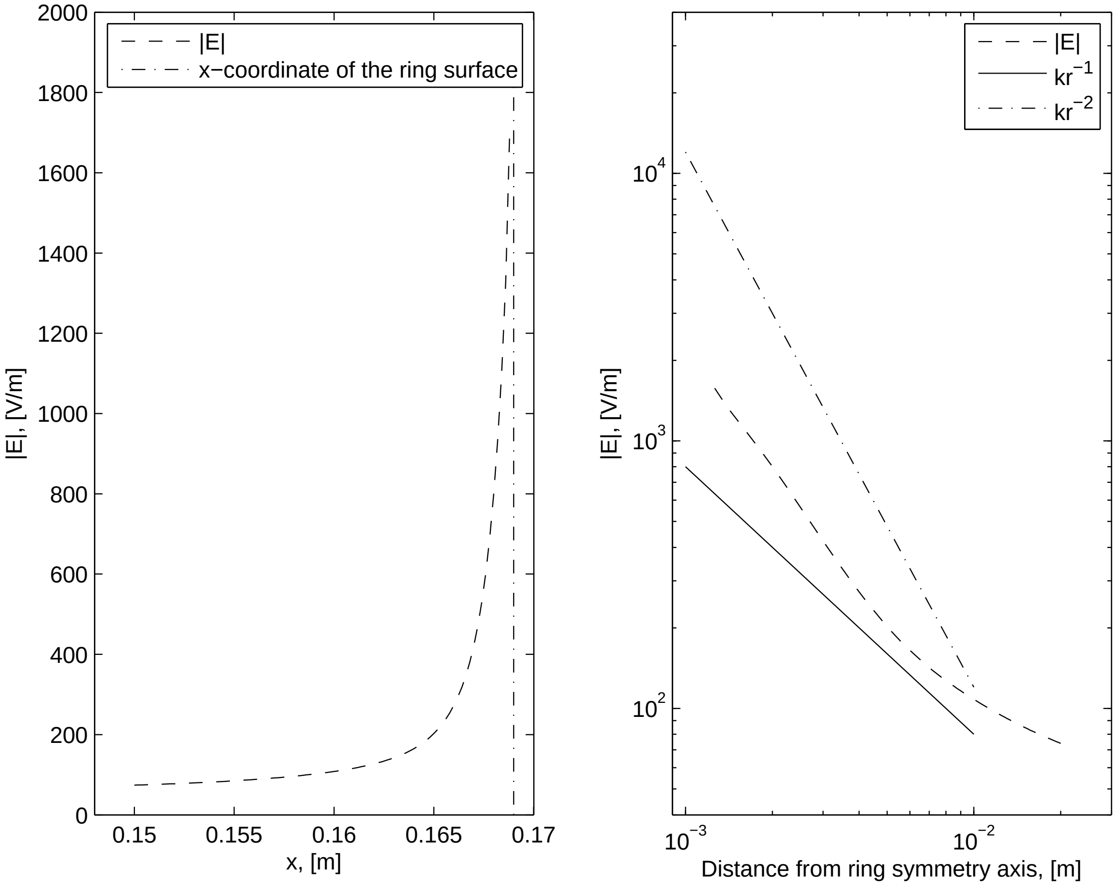

Figure 3.14. Amplitude of the electric field on a straight line perpendicular to the ring electrode as a function of x (*left*) and distance from the symmetry axis of the ring electrode (*right*). In the right hand plot, two functions proportional to r^{-1} and r^{-2} respectively have been added for comparison.

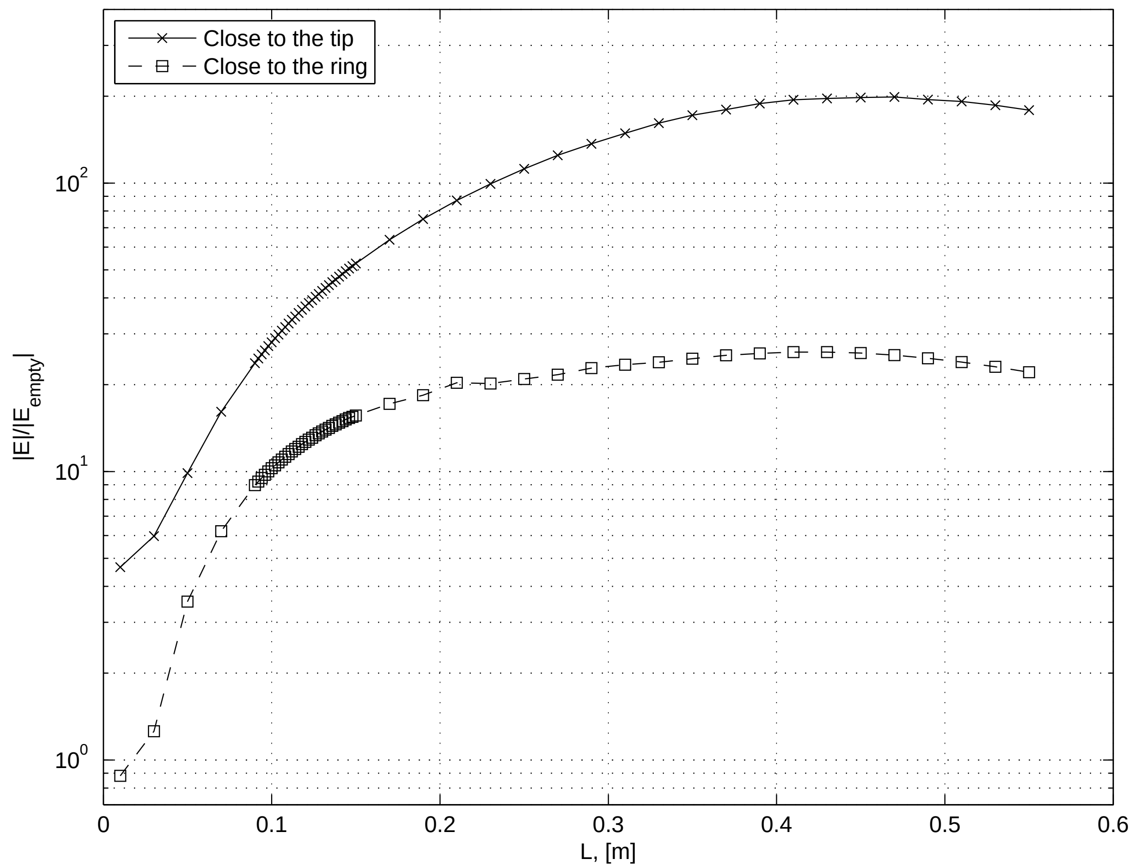

Figure 3.15. Amplification factor for the electric field amplitude close to the tip (*solid*) and ring (*dashed*) with respect to the empty case as a function of lead length.

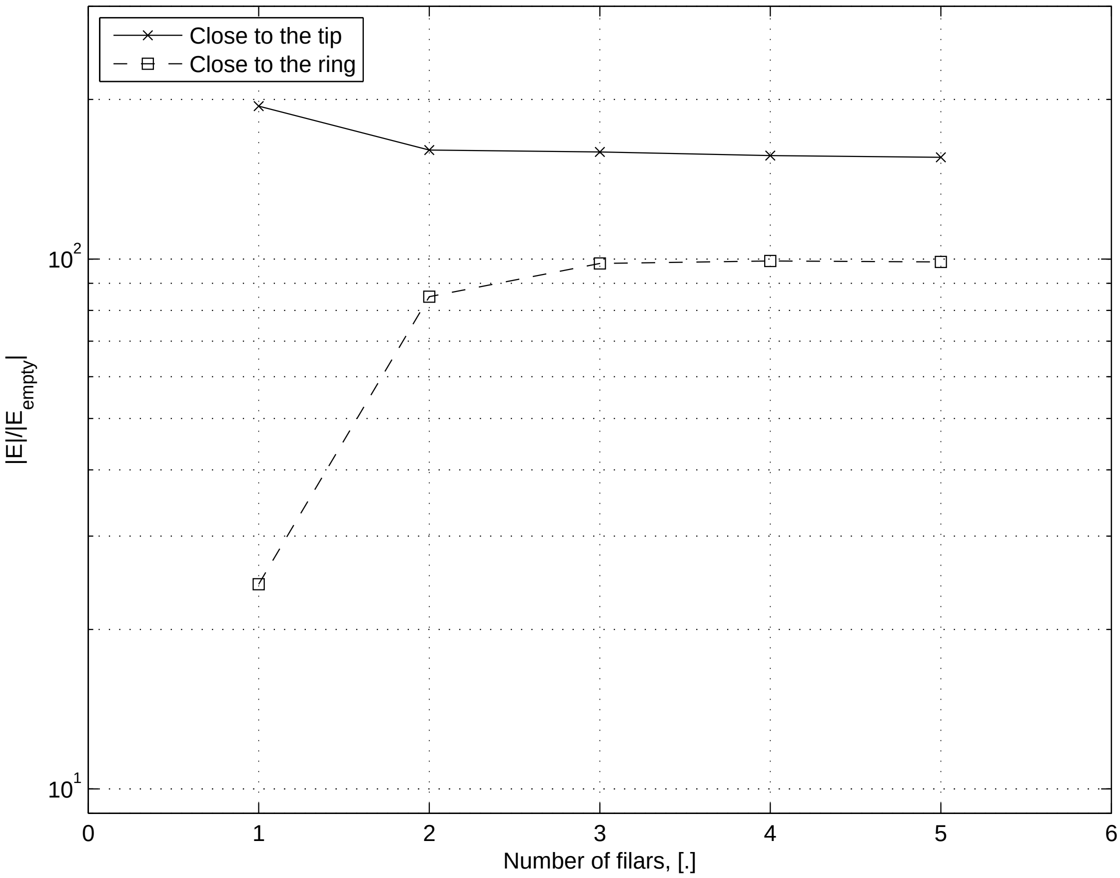

Figure 3.16. Amplification factor for the electric field amplitude close to the tip (*solid*) and ring (*dashed*) with respect to the empty case as a function of the number of conductor filars.

3.2.2 Impact of number of filars

Once again we depart from the standard setup described in table 2.3 and vary the number of filars in the conductors. The number of filars ranges from one to five and the same number of filars is used for both conductors. The pitch angle is kept constant regardless of the number of filars. Thus, the filars are more densly packed as their number increases.

The amplification factor of the electric field in the two test points near the tip and ring electrodes is presented in figure 3.16. As can be seen in the figure, the amplification factor is almost constant with respect to the number of filars near the tip electrode. Another behavior is shown by the amplification factor near the ring electrode, which increases with the number of filars.

Although the change in amplification factor near the tip is quite small, the induced current on the conductors is clearly different between the one-filar case shown in figure 3.17 and the five-filar case in figure 3.18. Whereas the current amplitude varies slowly in the one-filar case, a much more rapid-varying current pattern is

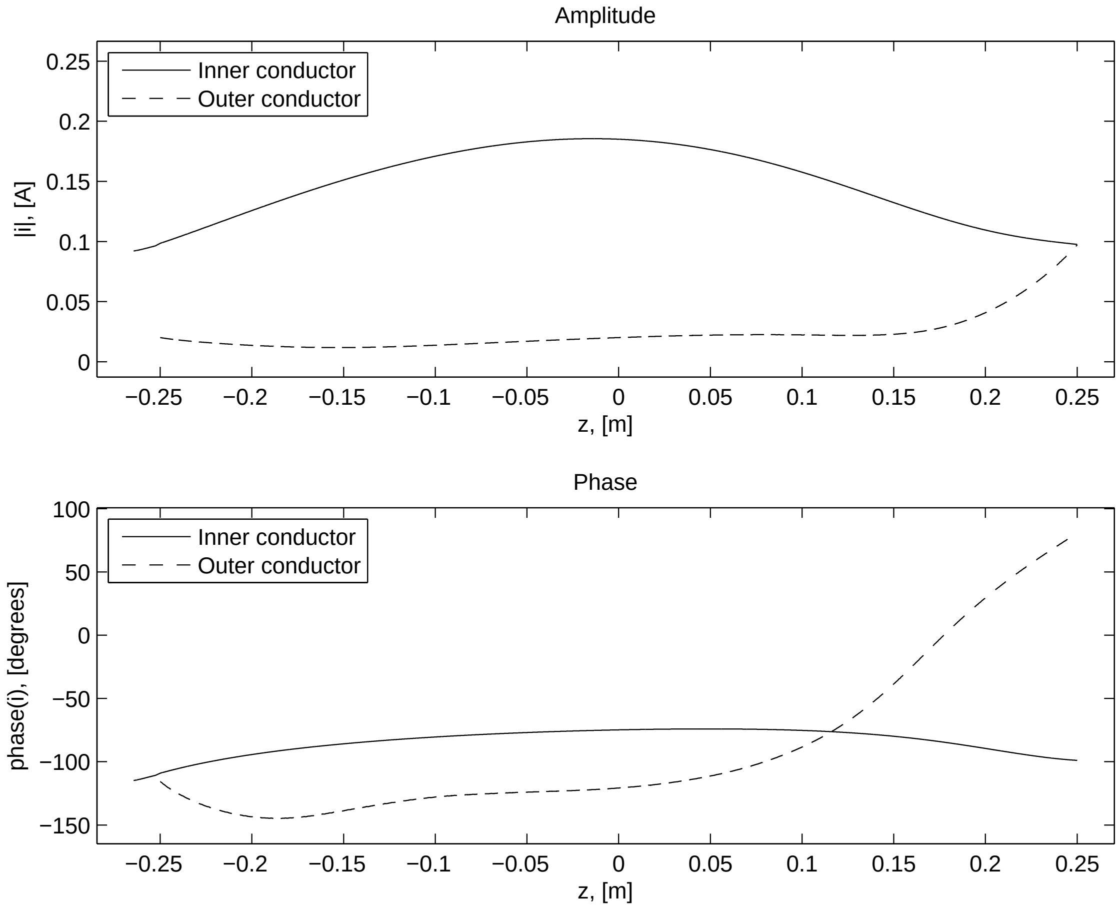

Figure 3.17. Amplitude (*top*) and phase (*bottom*) of the currents induced in the lead with 1 filar as a function of z.

present in the five-filar lead.

The difference in current on the filars of the outer conductor is due to discretization errors associated with the proximity to the surface of the insulation. This difference changes significantly with the number of segments N_s around the circumference of the insulation. The difference is substantially reduced for cases where N_s is a multiple of the number of filars.

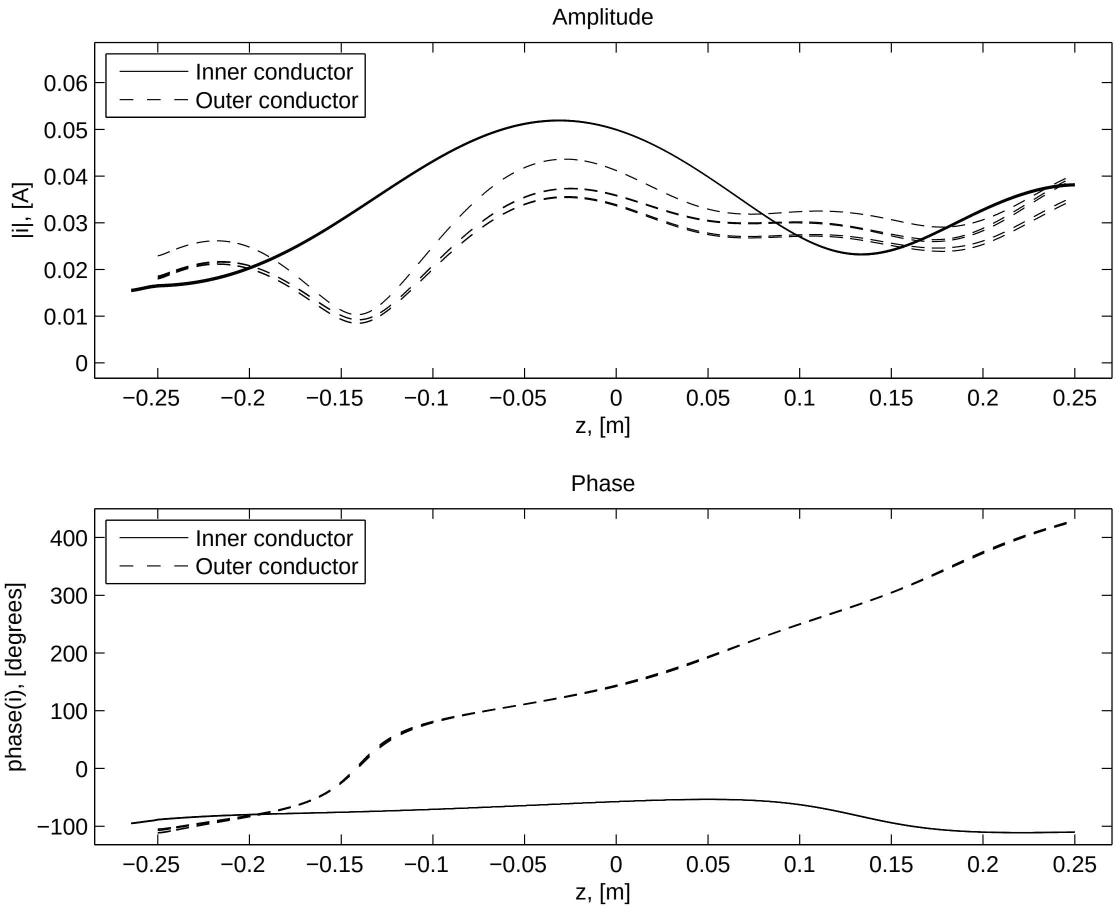

Figure 3.18. Amplitude (*top*) and phase (*bottom*) of the currents induced in the lead with 5 filars as a function of z. Note that there are five solid curves for each of the filars of the inner conductor in each plot and similarly for the outer conductor (dashed curves).

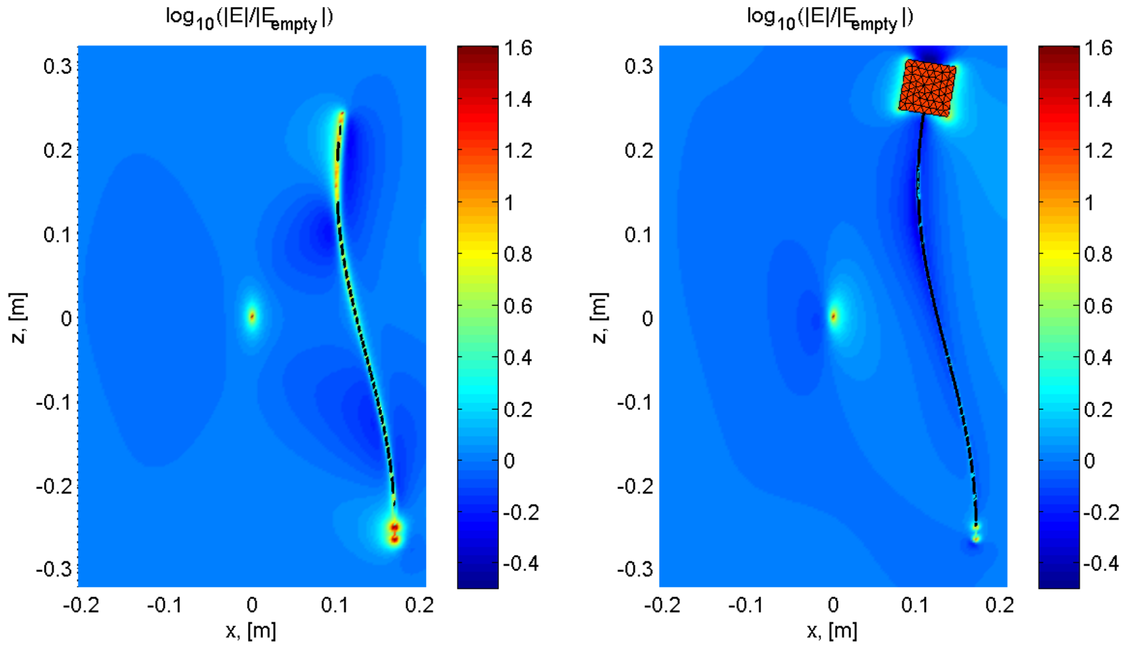

Figure 3.19. Amplification factor for the electric field amplitude with respect to the empty case around a curved lead in the plane $y = 0$ without (*left*) and with (*right*) a pacemaker unit. The lead conductors are wound in the same direction.

3.2.3 Impact of detailed modeling

A curved lead with three filars in both conductors is modeled both with and without a pacemaker unit. A lumped capacitance of 1 nF connects the inner and outer conductors at the pacemaker end of the lead. If the pacemaker unit is present, a similar capacitance connects the outer conductor to the pacemaker shell. The standard test case from section 2.3.5 is used with $x(s) = -0.07(1 - \cos(1.2\pi s))$, cf. table 2.3. Furthermore, the conductors are either wound in the same direction or in opposite directions.

The amplification factor around the entire pacemaker system is shown in figure 3.19 for a lead with conductors wound in the same direction and in figure 3.20 for a lead with conductors wound in opposite directions. The amplification factor is moderate around the pacemaker unit and, similarly to the test case above, the highest amplification occurs in the vicinity of the tip electrode. It should be noted that the electric field vanishes at the midpoint of the empty phantom, which causes the amplification factor to be misleading near this point.

The electric field amplification values evaluated at the test points are summarized in table 3.1 for the four combinations of conductor winding and pacemaker unit presence. The presence of the pacemaker unit has drastic influence on the evaluated electric fields and the currents induced on the conductors. The electric fields are reduced by a factor of $5 - 10$ by the presence of the pacemaker unit. Thus, it seems that the charges flowing in the implant prefer to accumulate on the large surface of

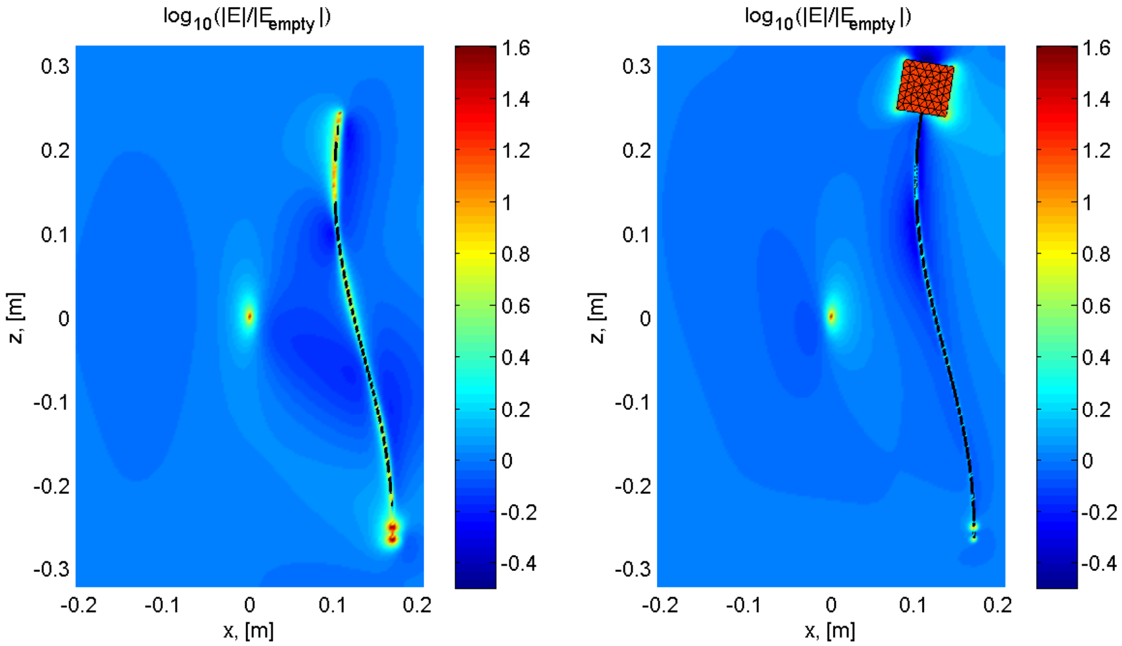

Figure 3.20. Amplification factor for the electric field amplitude with respect to the empty case around a curved lead in the plane $y = 0$ without (*left*) and with (*right*) a pacemaker unit. The lead conductors are wound in opposite directions.

Near the tip		
Winding	without PM	with PM
Same direction	113	22.7
Opposite directions	135	13.6
Near the ring		
Winding	without PM	with PM
Same direction	81.4	13.4
Opposite directions	83.8	16.3

Table 3.1. Amplification of the electric field in two points: one near the tip and one near the ring.

the pacemaker unit instead of along the lead and at its electrodes.

The conductor winding causes a change in the electric fields by a factor of $0.82 - 1.67$ where neither of the winding schemes produce consistently lower fields.

The currents induced on the conductors of the pacemaker-attached leads are shown in figure 3.21 for conductors wound in the same direction and in figure 3.22 for conductors wound in opposite directions. The corresponding currents for the abandoned leads are shown in figure 3.23 for conductors wound in the same direction and in figure 3.24 for conductors wound in opposite directions. As can be seen in the figures presenting the induced currents, the standing wave pattern changes significantly with the conductor winding and the presence of a pacemaker unit.

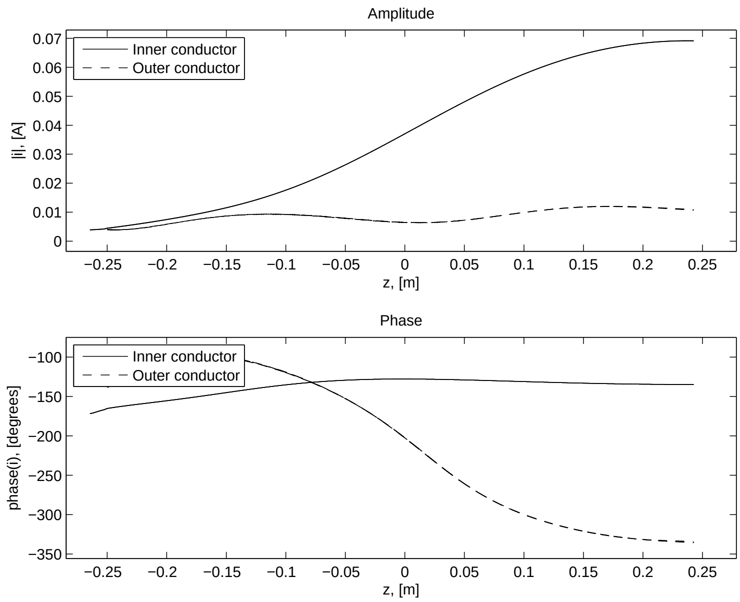

Figure 3.21. Amplitude (*top*) and phase (*bottom*) of the currents induced in a lead with 3 filars attached to a pacemaker as a function of z. The lead conductors are wound in the same direction.

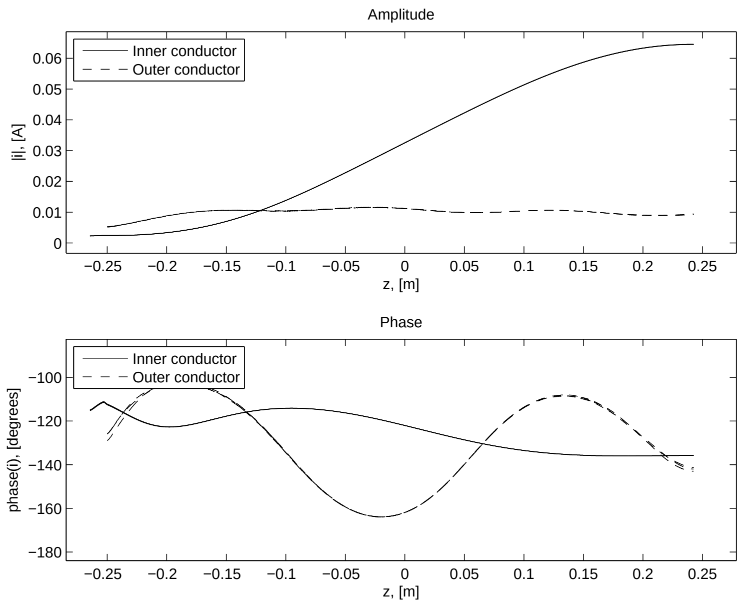

Figure 3.22. Amplitude (*top*) and phase (*bottom*) of the currents induced in a lead with 3 filars attached to a pacemaker as a function of z. The lead conductors are wound in opposite directions.

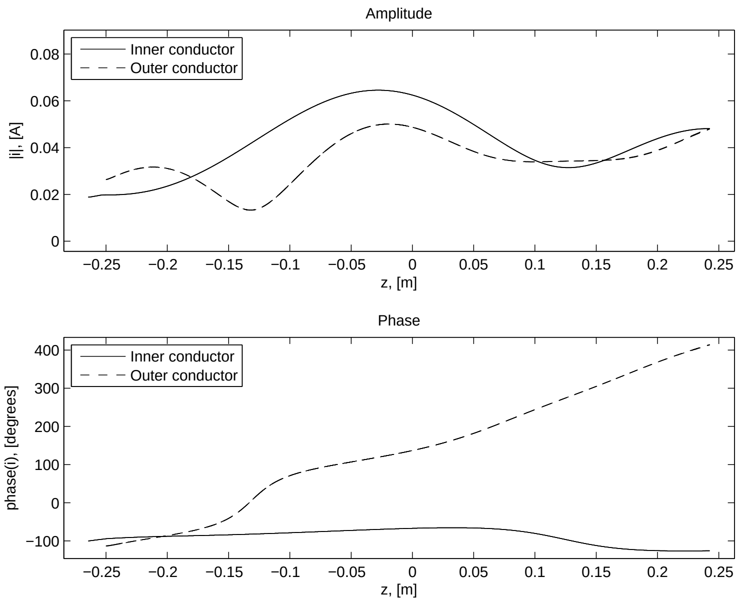

Figure 3.23. Amplitude (*top*) and phase (*bottom*) of the currents induced in an abandoned lead with 3 filars as a function of z. The lead conductors are wound in the same direction.

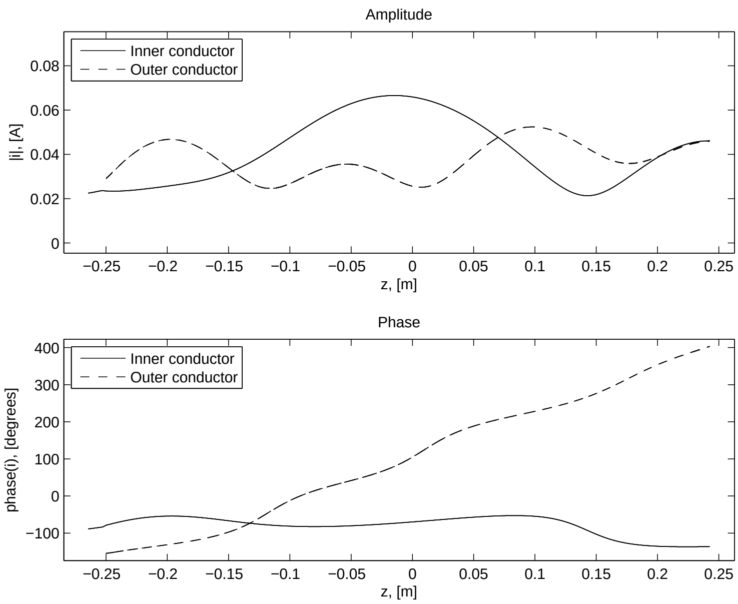

Figure 3.24. Amplitude (*top*) and phase (*bottom*) of the currents induced in an abandoned lead with 3 filars as a function of z. The lead conductors are wound in opposite directions.

4 Conclusion

In this work, the electromagnetic part of MR-induced pacemaker lead heating was investigated. The multi-scale part of the problem was taken into special consideration during the modeling process.

A setup inspired by the test standard ASTM F2182-09 [16] was modeled with the method of moments in frequency domain. The model included a generic RF birdcage coil, a human body phantom filled with a lossy dielectric as well as a pacemaker system. The pacemaker system consisted of a pacemaker unit and a highly detailed model of a bipolar lead including dielectric insulation, conductor filars, electrode surfaces and lumped components.

Several configurations of pacemaker systems exposed to MRI were modeled and factors like lead length, direction of conductor winding, number of filars, and pacemaker unit presence were studied. The corresponding results clearly showed the importance of detailed lead modeling. For example, the shape of the induced currents change considerably with the number of filars.

The lead modeling was based on the thin-wire approximation wherefore modeling of resonant structures with this approximation was investigated. Results obtained by surface discretization of the wires were used as reference. For closely positioned wires, the number of resonances and their frequencies can vary significantly between the two modeling approaches. Thus, great care must be taken in such situations, especially if a double helix is modeled.

Further improvements of the model are needed before a more substantial parameter study of the lead heating phenomenon can be fully utilized. Additional details, such as filars in electrical contact with each other, may also be added to the model.

Bibliography

[1] Medtronic. Revo MRI Pacing System. `www.medtronicexperience.com/ws/files/Client_74/Product_1010/Booth_1022/Module_1054/Asset_163/OverviewBrochure.pdf`, Accessed Oct. 5, 2011.

[2] St. Jude Medical. Tendril MRI Pacing Lead. `www.sjmprofessional.com/Products/Intl/Pacing-Systems/Tendril-MRI-Lead.aspx`, Accessed Oct. 5, 2011.

[3] Joseph F Zikria, Stephen Machnicki, Eugene Rhim, Tandeep Bhatti, and Robert E Graham. MRI of patients with cardiac pacemakers: a review of the medical literature. *AJR. American journal of roentgenology*, 196(2):390–401, February 2011.

[4] W. Liu, C. M. Collins, and M. B. Smith. Calculations of B1 distribution, specific energy absorption rate, and intrinsic signal-to-noise ratio for a body-size birdcage coil loaded with different human subjects at 64 and 128 MHz. *Applied Magnetic Resonance*, 29(1):5–18, March 2005.

[5] C.J. Yeung, R.C. Susil, and Ergin Atalar. RF safety of wires in interventional MRI: using a safety index. *Magnetic Resonance in Medicine*, 47(1):187–193, 2002.

[6] Christopher J Yeung, Robert C Susil, and Ergin Atalar. RF heating due to conductive wires during MRI depends on the phase distribution of the transmit field. *Magnetic Resonance in Medicine*, 48(6):1096–8, December 2002.

[7] S.M. Park, R. Kamondetdacha, and J.A. Nyenhuis. Calculation of MRI-induced heating of an implanted medical lead wire with an electric field transfer function. *Journal of Magnetic Resonance Imaging*, 26(5):1278–1285, 2007.

[8] S.M. Park. *MRI safety: Radiofrequency field induced heating of implanted medical devices*. PhD thesis, Purdue University, West Lafayette, Indiana, USA, 2006.

[9] Paul A. Bottomley, Ananda Kumar, William A. Edelstein, Justin M. Allen, and Parag V. Karmarkar. Designing passive MRI-safe implantable conducting leads with electrodes. *Medical Physics*, 37(7):3828–3843, 2010.

[10] Stefano Pisa, Paolo Bernardi, Marta Cavagnaro, and Emanuele Piuzzi. Power Absorption and Temperature Elevation Produced by Magnetic Resonance Apparatus in the Thorax of Patients With Implanted Pacemakers. *IEEE Transactions on Electromagnetic Compatibility*, 52(1):32–40, February 2010.

[11] Eugenio Mattei, Giovanni Calcagnini, Federica Censi, Michele Triventi, and Pietro Bartolini. Numerical model for estimating RF-induced heating on a

pacemaker implant during MRI: experimental validation. *IEEE transactions on bio-medical engineering*, 57(8):2045–52, August 2010.

[12] M.H. Vogel and R.P. Kleihorst. Large-Scale Simulations Including a Human-Body Model for MRI. *2007 IEEE/MTT-S International Microwave Symposium*, pages 1345–1348, June 2007.

[13] S.M. Park and M. Conroy. Electromagnetic Modeling of RF Induced Lead Heating - Ensuring MRI for Patients with Active Implanted Medical Devices. In *ISMRM Workshop on MR Safety: RF Heating of the Human in MRI, 2010*, `www.ismrm.org/workshops/Safety_10/program.htm`, Accessed Aug. 22, 2011.

[14] E Neufeld, S Kühn, G Szekely, and N Kuster. Measurement, simulation and uncertainty assessment of implant heating during MRI. *Physics in medicine and biology*, 54(13):4151–69, July 2009.

[15] O Talcoth, T Rylander, H S Lui, and M Persson. Monolithic multi-scale modeling of MR-induced pacemaker lead heating. In *2011 International Conference on Electromagnetics in Advanced Applications*, pages 599–602. IEEE, September 2011.

[16] *Standard Test Method for Measurement of Radio Frequency Induced Heating Near Passive Implants During Magnetic Resonance Imaging, Standard F2182-09.* ASTM International, West Conshohocken, PA, USA, 2010.

[17] Andreas Christ, Wolfgang Kainz, Eckhart G Hahn, Katharina Honegger, Marcel Zefferer, Esra Neufeld, Wolfgang Rascher, Rolf Janka, Werner Bautz, Ji Chen, Berthold Kiefer, Peter Schmitt, Hans-Peter Hollenbach, Jianxiang Shen, Michael Oberle, Dominik Szczerba, Anthony Kam, Joshua W Guag, and Niels Kuster. The Virtual Family–development of surface-based anatomical models of two adults and two children for dosimetric simulations. *Physics in medicine and biology*, 55(2):N23–38, January 2010.

[18] Efield AB. Efield 5.3. `www.efieldsolutions.com`.

[19] Efield AB. Efield 6.0 beta. `www.efieldsolutions.com`.

[20] Eugenio Mattei, Giovanni Calcagnini, Michele Triventi, Federica Censi, and Pietro Bartolini. Numerical FDTD models of electromagnetic field generated by the RF coil of an MRI scanner: comparison among different solutions. In *Proceedings of the Sixth IASTED International Conference on Biomedical Engineering*, pages 187–192. ACTA Press, 2008.

[21] J. M. Jin. *Electromagnetic analysis and design in magnetic resonance imaging.* Biomedical engineering series. CRC Press, Boca Raton, 1999.

[22] Comsol AB. COMSOL Multiphysics 4.0a. `www.comsol.com`.

[23] Anna Norlin. *Investigation of electrochemical properties and performance of stimulation / sensing electrodes for pacemaker applications*. PhD thesis, Royal Institute of Technology, Stockholm, Sweden, 2005.

[24] Christopher J. Yeung and Ergin Atalar. A Green's function approach to local rf heating in interventional MRI. *Medical Physics*, 28(5):826, 2001.